Dissertation
submitted to the
Combined Faculties for the Natural Sciences and for Mathematics
of the Ruperto-Carola University of Heidelberg, Germany
for the degree of
Doctor of Natural Sciences

presented by:

Diplom-Physicist: Simeon Nill
born in: Reutlingen

Oral examination: 31st October, 2001

Development and application of a multi-modality inverse treatment planning system

Referees: Prof. Dr. Thomas Bortfeld
Prof. Dr. Josef Bille

Zusammenfassung

Entwicklung und Anwendung eines multimodalen inversen Bestrahlungsplanungsystems

Mit der Einführung der intensitätsmodulierten Strahlentherapie (IMRT) eröffnen sich neue Möglichkeiten in der Bestrahlungsplanung. Die meisten bisher existierenden Bestrahlungsplanungsysteme (BP) für die IMRT sind konzeptionell ausschließlich für Photonen entwickelt worden. Dabei wurde der Schwerpunkt vor allem auf die Optimierung der Rechengeschwindigkeit gelegt, was zum Einsatz vereinfachter Dosisberechnungsmodelle und Näherungen in der Berechnung der Fluenzmatrizen führte. Das Ziel dieser Arbeit ist es daher, ein IMRT Bestrahlungsplanungsystem für den Einsatz beliebiger Strahlenarten mit verbesserten Dosisberechnungsalgorithmen zu entwickeln. Für das Dosisberechnungsmodul wird ein Verfahren entwickelt, bei dem der Dosisbeitrag in einem Voxel für jeden beliebigen Strahl vorausberechnet und in einer Matrix abgespeichert wird. Dadurch wird der Einsatz verbesserter Dosisberechnungsalgorithmen sowie die gleichzeitige Optimierung verschiedener Strahlenarten ermöglicht. Das neue BP wurde angewendet auf klinische Patientendaten zur Berechnung von Protonen- und Photonen-IMRT Plänen. Bei der Bestrahlung mit Protonen wurden zwei neuartige Techniken zur Spotpositionierung, die 3D Technik sowie das "distal edge tracking" (DET) miteinander verglichen. Dabei ergibt sich, dass die mit Hilfe der DET Technik erzielten Dosisverteilungen denen der 3D Technik entsprechen, aber um einen Faktor 10 schneller zu optimieren und voraussichtlich zu applizieren sind. Desweiteren wurde kein signifikanter Unterschied bei der Berücksichtigung von Organbewegungen und Reichweitenunsicherheiten zwischen den beiden Techniken festgestellt.

Abstract

Development and application of a multi-modality inverse treatment planning system

The introduction of intensity-modulated radiation therapy (IMRT) opened new possibilities for the treatment planning process. Most of the existing treatment planning (TP) tools for the IMRT are focusing on the use of photons for the treatment. To achieve a very high computional speed only simplified dose calculation algorithms are used. Furthermore, approximations are made during the calculation of the fluence matrix. This thesis develops an IMRT planning tool which can be used with any available radiation modality and makes use of improved dose calculation algorithms. For the dose calculation engine a method was developed where the dose deposited in every voxel by all beams is precalculated and for later use stored in a dose matrix. This enables the use of advanced dose calculation algorithms and the simultaneous optimization of different radiation modalities. The new TP system was applied to clinical patient data for proton and photon IMRT plans. For the delivery of the proton IMRT plans two promising delivery techniques, "distal edge tracking" (DET) and the 3D technique, were compared with each other. By using the DET technique dose distributions as good as for the 3D technique were achieved but the optimization time and the expected delivery time are reduced by a factor 10. In addition, no significant differences in the effect of organ motion and particle range uncertainties are observed for either technique.

Contents

Chapter 1

Introduction

With the development of the first intensity-modulated radiotherapy (IMRT) treatment planning system for photons, KonRad by Bortfeld et. al [6, 9], a new approach in radiotherapy for cancer was created at the German Cancer Research Center (DKFZ). Patients are normally treated with several beams coming from different directions to create a dose distribution around a common center of rotation (isocenter) [74,75]. By varying the intensity of every beam element (bixel) it is possible to generate dose distributions with a higher conformation to the target volume compared to conventional irradiation techniques, where only the weight of each beam can be optimized. This leads to a better sparing of the organs at risk (OAR) especially for concave target volumes surrounding the OAR. Another benefit of the IMRT technique is the possibility of escalating the dose in the tumor volume to achieve a better tumor control probability [44,51,57]. From 1995 to 2001 only a small fraction of all patients receiving radiotherapy were treated with IMRT. For these first patients the application of IMRT had to be done very carefully, requiring a lot of time, and careful quality assurance. Nevertheless, the use of IMRT will be more common in the near future [22].

The number of planning tools available to create IMRT treatment plans is large [1, 14, 18, 46, 56, 70], but most of the existing planning tools were designed to offer only one radiation modality mostly photons to the physicians. To reduce the computation time for the optimization process simplified dose calculation algorithms and approximations during the calculation of the bixel weights [56] are made. Therefore the use of different radiation modalities and more accurate dose calculation algorithms or even Monte Carlo or superposition algorithms is not possible within most of the existing IMRT planning tools.

To improve the quality of future IMRT treatment plans the use of more accurate dose calculation algorithms and the possibility to select different radiation modalities within the systems must be available. The achieve these aims a new multi modality inverse treatment planning tool was developed. A modular design between the three important parts of the program, the optimization loop, the dose engine and the graphical user interface for the new IMRT planning tool was achieved. This enables the easily extension or modification of one of the three modules of the system without the need to change any other part. Any module of the planning tool only communicates with the other parts through the pre-calculated D_{ij} matrix. Because the computational power and the amount of available memory in personal computers has increased a lot in the last few years it is now possible to use the D_{ij} dose matrix approach as the central component of the new planning tool.

By choosing the modular design and the D_{ij} dose matrix approach we show that it is now possible to use accurate dose calculations for the IMRT treatment planning process. Another important advantage of the D_{ij} matrix is the potential to use different radiation modalities within the IMRT treatment planning system. It is therefore not only possible to optimize for example protons but also to explore the potential of the simultaneous optimization of proton and photon treatments.

To test the potential of accurate dose calculation algorithms two dose calculation engines were built. First a photon dose calculation engine was developed and implemented to calculate the dose matrix [12]. Secondly, a dose calculation engine for heavy, charged particles was created [23, 28, 39, 50, 60, 64]. The system is not limited to these two dose engines. With the newly developed design any dose calculation can be attached to the system, for example a photon Monte Carlo or an electron pencil beam dose engine.

The first application of the new system was to two patient studies. One was treated for a prostate carcinoma and the second for a clivus chordoma. Both tumors are complicated to irradiate and should therefore be treated with IMRT. Optimized plans for photons, electrons, protons and carbon ions were calculated and are presented and discussed.

For the heavy, charged particles, especially protons, the differences between the available delivery technique (DET [21] and 3D [47]) are explored. To test the potential of these two new techniques treatment plans for a different number of beam directions were calculated and compared to each other and to photon IMRT plans. To evaluate the influence of the target motion on the optimized treatment plans the dose volume histograms are compared for different target positions.

For heavy, charged particles the calculated position of the Bragg peak inside the patients is of paramount importance. Every slight miscalculation or mispositioning of the peak position could lead to a different dose distribution. The uncertainties of the used relative stopping power [34, 61, 65] and the errors introduced by the treatment device [48] could lead to a misalignment of the beam spots. Therefore, the optimized treatment plans were recalculated with different relative stopping powers to analyze the effect on the dose distributions.

This thesis describes the development and application of a new multi modality inverse treatment planning system. In chapter 2 the new modular design and the D_{ij} matrix approach are explained. In chapter 3 the physical models used to create the D_{ij} matrix for photons and heavy, charged particles, especially protons, are developed and tested. Chapter 4 presents the first result of the new planning tool and explores the potential of the 3D and DET delivery technique for heavy, charged particles and the simultaneous optimization of protons and photons. In chapter 5 the implications of this thesis are discussed and the final conclusions are presented. A summary and outlook concludes the thesis.

Chapter 2

Design of the multi-modality treatment planning system

2.1 Overview of existing planning tools

Since the introduction of the intensity-modulated radiotherapy by Bortfeld et al. [6,9] and the development of the first IMRT planning tool by Preiser et al. [56] other radiation planning systems have been developed. In table 2.1 the most frequently used IMRT planning tools for photons and in table 2.2 some of the available IMRT systems for heavy, charged particles are listed.

Most of the existing planning tools are only able to optimize one radiation modality within the same system. Only Korevaar et al. [38] can optimize electron and photon IMRT plans at the same time. In order to compare possible IMRT plans using different radiation modalities, like protons or photons [19, 48, 49, 52], two

Name	Company or research facility	Reference
KonRad	DKFZ, MRC	[56]
Corvus	Nomos	[18]
Helios	Varian	[70]
Pinnacle	Adac	[14]
-	Sweden	[46]
Hyperion	Tübingen	[1]

Table 2.1: *Overview over the most frequently used IMRT planning tools for photons.*

Name	Company or research facility	Radiation modality	Reference
TRIP	GSI	Carbons	[39]
-	PSI	Protons	[47]
-	Sweden	Protons	[16]
KonRad2	DKFZ	Multi modality	[53]

Table 2.2: *IMRT planning tools for heavy, charged particles.*

different planning systems with different optimization algorithms must be used. This makes comparison of the results very difficult. A comparison within the same system would be preferable, and would eliminate possible errors due to the use of different optimization algorithms.

2.2 Why another planning tool?

The answer to this question is to overcome the existing limitations of available IMRT treatment planning systems. As mentioned in section 2.1 it is not possible with most other treatment planning tools to optimize and compare different radiation modalities within a single system. However there are other disadvantages which are more serious. One is the use of less accurate photon dose calculation models to save computing time during the optimization process. This compromises the quality of the treatment plans. For example the scattering of photons is only taken into account in the dose calculation but not in the optimization of the bixel weights. See section 2.4.1.3 for a more detailed explanation.

In most other IMRT planning tools the dose calculation and the optimization loop are merged together to save computing time (see figure 2.4(a)). Therefore it is not easily possible to change either the dose calculation engine or the optimization algorithm without a major revision of the planning tool like rewriting and redesigning a significant part of the source code.

The goal of the new multi-modality IMRT treatment planning system is to overcome these limitations by using the developed D_{ij} matrix approach. This is now possible because the new personal computers and workstations are more powerful and provide a larger amount of memory. By using the D_{ij} matrix approach it is now possible to overcome the known limitations of the existing planning tools, especially the use of accurate dose calculations and scatter corrections already during the optimization loop.

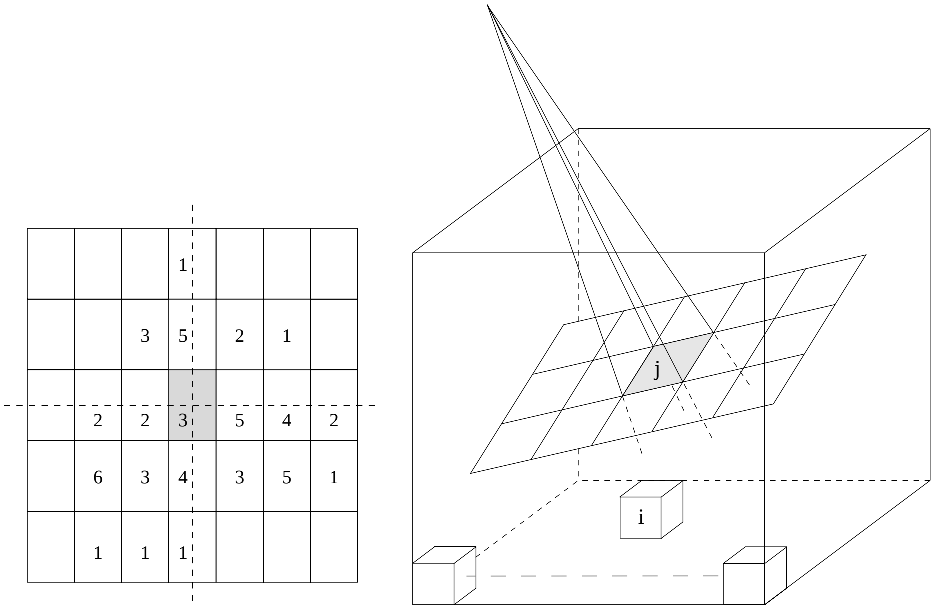

(a) *Isocenter plane* (b) *CT Cube*

Figure 2.1: *Definition of the D_{ij} matrix. (a) The isocenter plane is divided into small elements (bixels). Each bixel has an individual weight w_j (e.g. given by the numbers in the bixels) (b) Schematic view of a CT cube. The dose deposited by bixel j in voxel i is stored in the D_{ij} matrix at column j and row i.*

2.3 The D_{ij} matrix approach

The basic information for any planning system is the 3D data set from the computed tomograph (CT). The 3D CT data is divided into small volume elements of a given resolution called voxels. A typical voxel has a transverse dimension of about 2 mm and a height of 3 mm in the slice direction. The next step is the correlation of every voxel to a volume of interest (VOI). A VOI can be an organ at risk, normal body tissue or tumor volume. For this segmentation, a physician draws a 2D polygon contour in every transverse CT slice to define the different VOIs.

After this correlation, the different incident beam directions are chosen (see figure 2.1(b)). The fluence matrix is defined separately for each beam in the isocenter plane. The isocenter plane is perpendicular to the beam direction and contains the isocenter position. The fluence in the isocenter plane is divided into small elements called bixels (see figure 2.1(a)). Each bixel has its own weight w_j. The size of the bixels is defined by the user. The selected bixel or spot size depends on the radiation modality and the treatment device. The weights w_j of all bixels are optimized individually.

Therefore, the dose d_i at a given voxel i is the linear superposition of the dose delivered by all bixels. This can be written mathematically as

$$d_i = \sum_{j=1}^{N_j} D_{ij} w_j \tag{2.1}$$

$$\vec{d} = D\vec{w}, \tag{2.2}$$

where N_j is the number of bixel elements used during the treatment plan optimization. The D_{ij} matrix is the central component of the new planning tool. The matrix contains all necessary information to calculate the whole physical dose distribution. The column j in the D_{ij} matrix describes the 3D dose distribution originating from the bixel j. The dose deposited at the voxel position i from the bixel j is therefore stored in the D_{ij} matrix at column j and row i. Any type of dose calculation algorithm can be used to create the D_{ij} matrix.

Once the D_{ij} matrix has been calculated, dose calculation inside the optimization loop is very fast because only a matrix multiplication has to be done (see figure 2.4(b)). With this approach, accurate and time consuming dose calculations like Monte Carlo or superposition algorithms can be integrated into the treatment planning system. Additionally, it does not matter which dose calculation engine has created the D_{ij} matrix for the given bixel j. It is possible for the photon dose engine to create the columns for the photon bixels and the proton engine to create the columns for the proton spots. Simultaneous optimization of an arbitrary number of radiation modalities is consequently no problem.

The disadvantage of the D_{ij} matrix approach is the amount of required computer memory. In table 2.3 the required memory is listed for three sample IMRT plans. Todays workstations or even personal computers can handle up to two gigabytes of RAM with no problems. In the near future PCs will be able to handle more than four gigabytes.

To save computer memory only a reduced matrix is stored in the computer memory. There are two ways to select the element of the D_{ij} matrix which must be stored in the computer memory. First only elements with a dose value above a selected threshold T are taken into account:

$$D_{ij} \geq T. \tag{2.3}$$

Radiation	Photons	Protons DET	Protons 3D
Nr. of Beams	7	7	7
Bixel size [mm]	10x10	-	-
Bixels per beam	100	700	7000
Voxels per bixel	200000	4000	4000
Memory usage [MB]	840	118	1176

Table 2.3: *Required memory for the D_{ij} matrix for a typical photon IMRT plan and two different proton delivery techniques. For each D_{ij} matrix element 6 bytes of computer memory is allocated (Voxel resolution is $2.5\,mm^3$).*

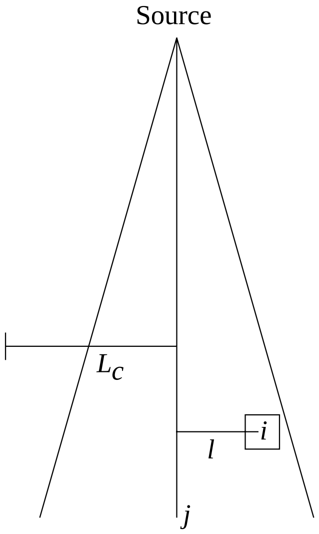

Figure 2.2: *Lateral cutoff calculation. If the distance l between the central ray of the bixel j and the center of the voxel i is larger then L_c the voxel is not stored inside the D_{ij} matrix.*

A second possibility is to define a lateral cutoff L_c. Only voxels with a distance l from the central ray of the bixel j (see figure 2.2) smaller then the lateral cutoff L_c are stored:

$$l \leq L_c. \tag{2.4}$$

The lateral cutoff L_c must be selected carefully to not introduce a systematic error into the dose calculation. L_c is set individually for every radiation modality and energy.

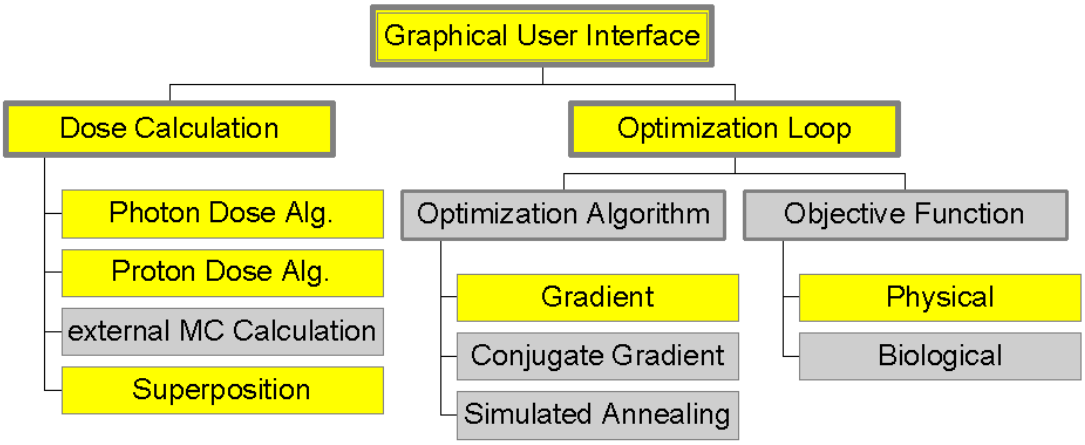

Figure 2.3: *Schematic overview of the developed IMRT planning tool. There is a strict separation between the graphical user interface, the dose calculation engine and the optimization loop. Each module can easily be replaced without the need to change anything in the other part of the system. The yellow boxes represents modules which are available.*

The lateral cutoff and threshold methods [20] are not the only methods which are available to reduce the amount of needed computer memory. The technique of stochastic sampling of the D_{ij} matrix reduces the number of elements [71] as well.

2.4 Design of the planning tool

The focus during the development and implementation of the new IMRT planning tool was to create a system which is modular and keeps a strict separation between the three main modules of every treatment system. First there is the optimization part. The optimization engine, is responsible for the calculation of the weights w_j for the optimal treatment plan. The only information which is shared between this module of the planning tool and the second important section, the dose engine, is the D_{ij} matrix. The third part of the system is the graphical user interface (GUI). An overview of the planning tool structure is shown in figure 2.3.

By choosing a modular approach any part of the system can later be replaced by a more sophisticated version without the need to redesign the whole system.

2.4.1 The optimization engine

The optimization engine is split into three parts:

1. The objective function.
2. The optimization algorithm.
3. The optimization loop.

For any section of the optimization engine different possibilities are available [6, 16, 27, 46, 47, 70, 76, 77, 79]. For the first implementation of the new IMRT planning tool the following selection was made.

2.4.1.1 The objective function

The goal of every IMRT planning tool is to produce a plan which is as close as possible to the requirements set by the physicians. To measure the difference between the treatment plan achieved and the prescribed dose distribution a mathematical norm must be defined. In this thesis, as in the implementation of most other treatment system, [18, 56, 70] the quadratic norm was used [9]. For every target volume t the user defines a minimum (d_t^{min}) and maximum (d_t^{max}) dose which should be applied to the target. Also a penalty (s_{u}^t) for under- or overdosage (s_{o}^t) is specified. The objective function for the target is then given by

$$F_t = \sum_i^{N_t} s_{\text{u}}^t [d_t^{\text{min}} - d_i]_+^2 + s_{\text{o}}^t [d_i - d_t^{\text{max}}]_+^2, \tag{2.5}$$

where d_i is the dose at the target voxel i and N_t are the number of voxels for the target t.

$[\cdot]_+$ is the positive operator which is defined as

$$[x]_+ = xH(x) = \begin{cases} x & x \geq 0 \\ 0 & \text{else} \end{cases} \tag{2.6}$$

For the organs at risk (OAR) (r) another objective function is defined:

$$F_r = \sum_i^{N_r} s_{\text{o}}^r [d_i - d_r^{\text{max}}]_+^2. \tag{2.7}$$

$d_r^{\max}$ is the maximum dose which is allowed for the organ at risk r. s_0^r is the penalty for overdosage and N_r is the number of voxels which belong to the organ r.

The complete objective function is then given by the sum over the number of targets N^{TARGET} and organs at risk N^{OAR}:

$$F = \sum_{t}^{N^{\mathrm{TARGET}}} F_t + \sum_{r}^{N^{\mathrm{OAR}}} F_r. \tag{2.8}$$

The concept of penalizing only under- or overdosage of a defined volume can be extended by the introduction of dose volume constraints into the objective function [13].

2.4.1.2 The optimization algorithm

The optimization algorithm is the essential part of the optimization engine. By using iterative [6] or stochastic methods [73] the weights of the bixels w_j are updated to find the optimal treatment plan. By using the modular approach any optimization algorithm could be integrated into the planning system. In the following sections the iterative gradient approach which is implemented into the new planning tool is explained in greater detail. Experience with the iterative Newton gradient approach in the predecessor of the new planning tool has shown that this optimization algorithm is a very fast and robust method. An overview of existing optimization algorithms can be found in Holmes et al. [27].

In this thesis a modified Newton gradient approach was used to update the weights of the bixels.

The dose d_i for any voxel i is given by

$$d_i = \sum_{j=1}^{N_j} D_{ij} w_j. \tag{2.9}$$

Using a generalized objective function, the derivatives of the function for the voxel i with the penalty factor s_i and the prescribed dose d^{pres} can then be calculated by

$$\begin{aligned} f_i =& s_i[d_i - d_i^{\text{pres}}]^2 && (2.10)\\ F =& \sum_i f_i && (2.11)\\ \frac{\partial f_i}{\partial d_i} =& 2 \cdot s_i \cdot [d_i - d_i^{\text{pres}}] && (2.12)\\ \frac{\partial^2 f_i}{\partial d_i^2} =& 2 \cdot s_i. && (2.13) \end{aligned}$$

By using the Newton gradient approach the result for the weights is then

$$\begin{aligned} w_j^{t+1} =& \left[w_j^t - \alpha \frac{\frac{dF}{dw_j}}{\frac{d^2F}{dw_j^2}} \right]_+ && (2.14)\\ \frac{dF}{dw_j} =& \sum_k \frac{\partial F}{\partial d_k} \frac{\partial d_k}{\partial w_j} && (2.15)\\ =& \sum_k 2 s_k [d_k - d_k^{\text{pres}}] D_{kj} && (2.16)\\ \frac{d^2F}{dw_j^2} =& 2 \cdot \sum_k s_k D_{kj}^2, && (2.17) \end{aligned}$$

with α as a normalization factor.

The result of this calculation is a procedure describing how to update the weights in every iteration step:

$$w_j^{t+1} = \left[w_j^t - \alpha \frac{\sum_i 2 s_i [d_i - d_i^{\text{pres}}] D_{ij}}{2 \sum_i s_i D_{ij}^2} \right]_+ . \qquad (2.18)$$

It is important to remember that the information required to evaluate equation 2.18 can be obtained by using the pre-calculated D_{ij} matrix. The calculation of the updated weights w_j^{t+1} can be done very fast because equation 2.18 contains no computationally time-consuming terms.

The only unknown variable in equation 2.18 is the normalization factor (damping factor) α. The following procedure is used to determine the factor:

1. Set all weights w_j^0 to zero and $\alpha = 1$.
2. Calculate the weights w_j^1 by using equation 2.18.
3. Calculate the mean dose in the target volume $D_t^{\text{mean,actual}} = \frac{1}{N_t} \sum_i^{N_t} d_i$ and $D_t^{\text{mean,pres}} = \frac{1}{N_t} \sum_i^{N_t} d_i^{\text{pres}}$.

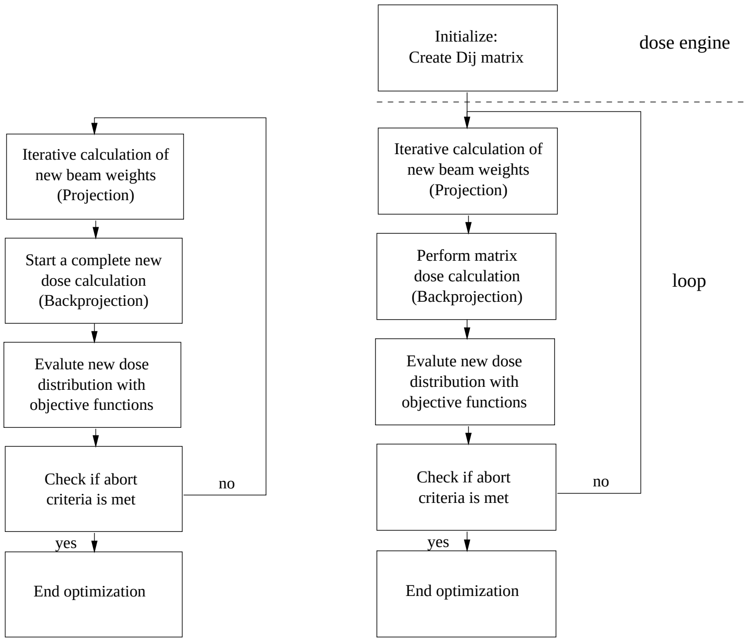

(a) *Integrated optimization and dose calculation.*

(b) *Modular optimization loop.*

Figure 2.4: *Optimization loops. (a) In this optimization loop a complete dose calculation must be performed in every iteration step. (b) After the initial calculation of the D_{ij} matrix the dose calculation step, the optimization loop is a fast matrix multiplication and a complete dose calculation is not required.*

4. Set the damping factor to $\alpha = \frac{D_t^{\mathrm{mean,pres}}}{D_t^{\mathrm{mean,actual}}}$.

If the damping factor is not set appropriately, the objective function will not converge.

2.4.1.3 The optimization loop

The optimization loop is an important part for every IMRT planning tool. After the user has specified all required information, the optimization loop takes over. First the dose engine is called to calculate the D_{ij} matrix for the given beam and radiation modality. This step is only done once. The next step in the optimization loop is to update the beam weights. The iterative equation 2.18 is used to calculate the new weights. The next step is to calculate the new 3D dose distribution with equation 2.2. Thereafter the value of the objective function is calculated. If the percentage difference between the current and the previous objective function value is smaller than a user defined threshold, the optimization loops stops, otherwise the next beam weights are calculated. See figure 2.4 for a schematic overview of both optimization loops.

The major difference between the optimization loop of the integrated IMRT tool and the modular system is the second step inside the loop. In the integrated optimization loop a complete dose calculation must be performed during each iteration step. For photons, for example, a pencil beam dose calculation which includes scattering is done. This takes only a few seconds but must be done in every iteration step. With the integrated loop Monte Carlo or superposition dose calculation could not be used within the IMRT systems because of the long time these dose calculations need. In the modular optimization loop the dose calculation is only a matrix multiplication which can be done in seconds. This time is independent of the dose calculation method and makes it possible to use Monte Carlo or superposition, since the real dose calculation (creation of the D_{ij} matrix) is done in advance. The time to create a superposition D_{ij} matrix is not important for the time the loop needs to find the optimal solution since the matrix is only calculated once before the loop starts.

Another disadvantage of the integrated loop in most treatment planning systems is that, for the photons, scattering is not handled completely correctly by the system. The dose calculation includes scattering, but during the updating of weights (projection), scattering is not taken into account. Again the modular optimization loop includes the scatter correction in the projection and the backprojection because in both steps the D_{ij} matrix is used.

2.4.2 The dose engine

The second but most important part of the new multi-modality planning system is the dose engine. The task of the dose engine is to create the D_{ij} matrix. Since the planning tool can handle more than one radiation modality at the same time, the dose engine is responsible for calling the correct dose calculation algorithm for every bixel. With this design it is also possible to mix different dose calculation algorithms for the same radiation modality, e.g. superposition and pencil beam algorithms.

To save valuable computer time and memory the D_{ij} matrix is stored as a compact matrix $\tilde{D}_{ij}$. Every element in the $\tilde{D}_{ij}$ matrix needs only six bytes. Four bytes are used to keep track of the voxel position inside the dose cube. To save computer memory the value of the matrix element is only stored by a two byte short integer value with ranging from 1 to 10000. To convert the short value into a real dose

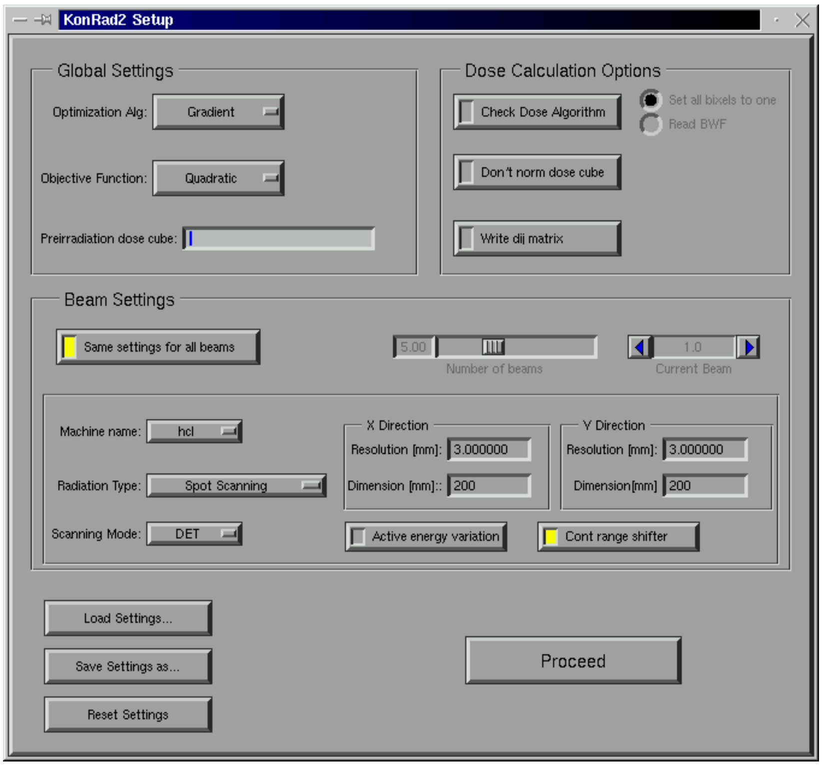

Optimization Alg: Gradient

Objective Function: Quadratic

Preirradiation dose cube:

☐ Check Dose Algorithm

● Set all bixels to one

○ Read BWF

☐ Don't norm dose cube

☐ Write dij matrix

☑ Same settings for all beams

5.00 Number of beams

1.0 Current Beam

Machine name: hcl

Radiation Type: Spot Scanning

Scanning Mode: DET

X Direction: Resolution [mm]: 3.000000

X Direction: Dimension [mm]:: 200

Y Direction: Resolution [mm]: 3.000000

Y Direction: Dimension[mm] 200

☐ Active energy variation

☑ Cont range shifter

Figure 2.5: *The new extension to the graphical user interface of the existing planning tool.*

value, a calibration factor c_j is stored only once for every bixel. The real value matrix element can then calculated by

$$D_{ij} = c_j \cdot \tilde{D}_{ij}. \tag{2.19}$$

By using only six bytes for every D_{ij} matrix element, instead of the conventional eight bytes (four bytes for the value and four bytes for the index), memory usage is reduced by 25%.

See figure 2.3 for an overview of the available dose calculation algorithms. The photon and proton pencil beam algorithms are explained in detail in chapter 3.

2.4.3 The graphical user interface

The graphical user interface of the prior version was changed simply to give the user access to the new options available (see figure 2.5). In this way physicians will be able to make use of the new system within a short period of time because they do not have to learn how to use a complete new system.

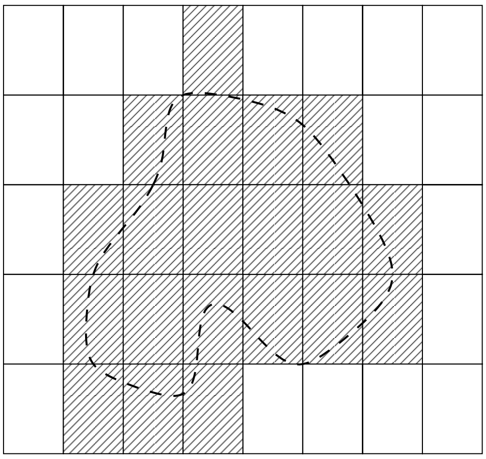

Figure 2.6: *The dashed line is the projection of the target volumes into the isocenter plane. The regular grid (solid lines) is defined in one direction by the leaf size and by the user in the other direction. Only shaded bixels are taken into account during the optimization.*

The new user interface enables the user to select an individual radiation modality and delivery technique for every beam. The bixel and scanning resolution can also be set. From the developer´s point of view, there was no need to rewrite the working components of an established planning system like the display of the computed tomography slices or the dose volume histograms.

2.5 Dose delivery modes

How the calculated fluence profiles are delivered to the patient depends mostly on the radiation modality used. The treatment device used limits the possible positions and the number of the bixel elements. In the following section the algorithm for calculating the bixel positions is explained for the two delivery systems used most frequently.

2.5.1 Multileaf collimators

Multileaf collimators (MLC) are used mostly to deliver the optimized IMRT treatment plan for photons and for electrons. An overview of the existing delivery modes like step & shoot or dynamic MLC movement can be found in the book of S. Webb [74]. For the calculation of the bixel positions the MLC mode used is irrelevant.

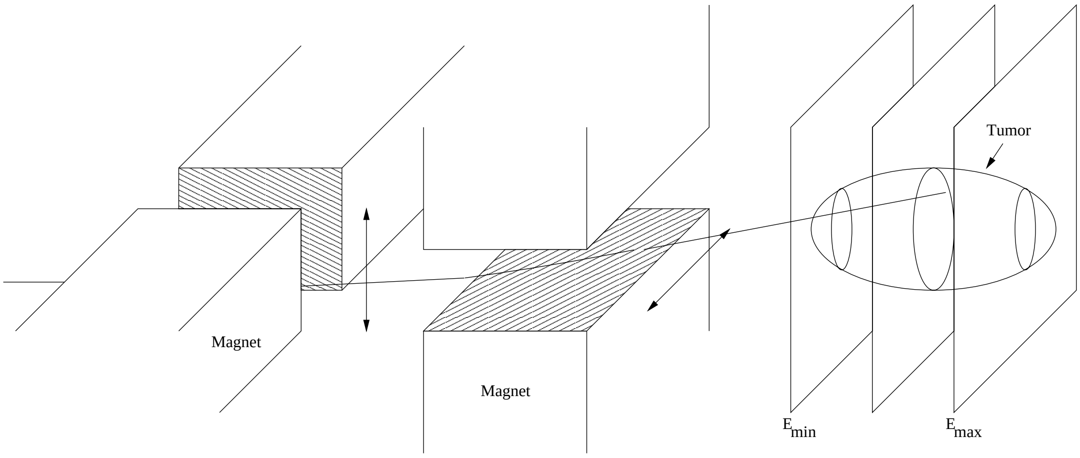

Figure 2.7: *Schematic view of a heavy, particle scanner: The two magnets control the lateral scan position of the particle beam. The target is divided into isoenergy slices. The range of the particle beam is controlled by the energy selection system.*

For every photon or electron beam the target volumes (3D) are projected onto the isocenter plane (2D). The isocenter plane is defined as the plane which contains the rotation center and is perpendicular to the beam. This is the same concept as used in the beam's eye view [4] in any other treatment system. This 2D polygon is then divided into bixels on a regular grid. The grid size is defined in one direction by the leaf width measured in the isocenter plane and in the other direction by the user. Any bixel which intersects the 2D polygon is taken into account during the optimization. Later the dose engine is responsible for creating the D_{ij} entries for these bixels.

2.5.2 The spot scanning system

To deliver intensity-modulated heavy, charged particles, a spot or raster scanning device [26, 50, 55, 63] is used at the following centers:

- the Paul Scherrer Institute (PSI), Villingen, Switzerland
- the Gesellschaft für Schwerionenforschnung (GSI), Darmstadt, Germany
- the Northeastern Proton Therapy Center (NPTC), Boston, USA

Figure 2.7 is a schematic overview of a scanning device. The target to be irradiated is divided into isoenergy planes. An isoenergy plane contains all positions

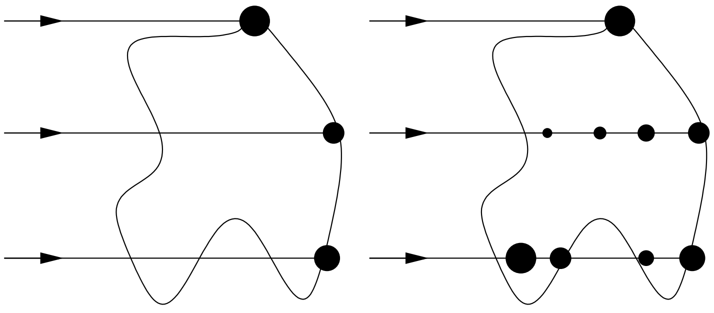

(a) *DET* (b) *3D*

Figure 2.8: *Two possible proton delivery techniques: (a) Distal edge tracking technique [21]. Spots are only placed at the distal edge of the tumor (b) 3D technique [16, 17]. Spots are placed all over the tumor. The radii of the spots show the intensity of the different proton spots.*

inside the patient which can be treated with the same particle energy. For every selected energy the particle beam has a well defined range. To change the range, either the energy of the beam must be changed (active energy variation) or some absorber material (range shifter) can be placed into the beam (passive energy variation) to reduce the range. The lateral steering of the particle beam is achieved by two magnets.

To treat a patient with a scanning device many beam spots are placed at different positions inside the target. According to Lomax et al. [47] there are four different IMRT spot scanning delivery methods (2D, 2.5D, 3D, DET). The main difference between these techniques is the position and the number of used beam spots. This thesis only focus on the two most promising methods, the distal edge tracking and the 3D technique. The 2D and 2.5D techniques are omitted, because they have a limited number of degrees of freedom.

1. The distal edge tracking technique (DET)
   The beam spots used by the distal edge tracking technique [21] are only placed at the distal edge of the target (see figure 2.8(a)). To track the distal edge of the tumor, either an active energy variation or different range shifter must be used for every spot. For the lateral distribution of the beam spots a regular grid are used.

2. The 3D technique (3D)
   For the 3D technique [16, 17] the beam spots are not only placed at the distal edge of the tumor but also inside the tumor (see figure 2.8(b)). The

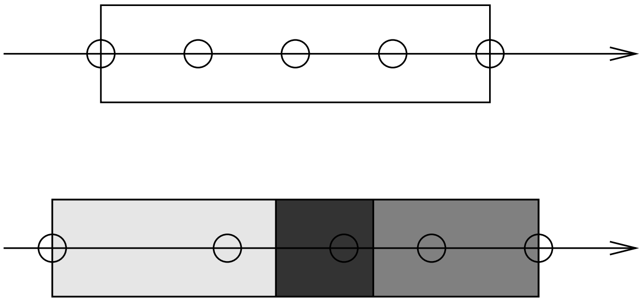

Figure 2.9: *3D beam spot positions: A radiological depth axis is used for the upper part of the plot. The 3D spots are placed on an equidistant grid. For the second plot a geometrical depth axis is used. The distance between the spots is therefore no longer equidistant.*

spot positions used inside the tumor mainly depend on the scanning device. The planning tool must take the available energies or range shifter positions of the scanning device into account during the calculation of the 3D spot positions inside the tumor.

The weight of every beam spot is optimized individually.

2.5.2.1 How to find the spot positions

The selection of the spot positions is done automatically by the planning tool. The user has only to define the delivery technique and the lateral distance of the beam spots in the isocenter plane.

1. First a raytracing [67] is done through the CT-cube starting at the source of the beam. The direction of the ray is given by the lateral coordinates of the beam spot, defined in the isocenter plane.
2. The radiological depth for any point along the ray is calculated. For every voxel the Hounsfield units from the CT scan are converted into relative stopping power S_{rel} with the help of a conversion table. The radiological depth η for a depth d is given by

$$\eta(d) = \int_0^d S_{\mathrm{rel}}(x)dx. \tag{2.20}$$

3. To find the distal edge of the tumor the radiological depth is analyzed for every voxel which intersects with the beam ray. The tumor voxel with the

> largest radiological depth defines the distal edge for this spot. The tumor voxel with the smallest radiological depth defines to position of the proximal edge of the tumor.

This procedure is carried out for every lateral beam spot position. If no distal edge can be found the spot position is discarded and not taken into account during optimization.

For the 3D technique another step is necessary to calculate the beam spot positions inside the tumor. With knowledge of the radiological depth of the proximal and distal edge of the tumor, new spots are placed in between these two positions. The new spots are placed on a radiological depth grid. The grid resolution is either user-defined or predefined by the scanning device.

It is important to keep in mind that spots are placed on a radiological and not a geometrical grid. For example if the distance between two spots is given by the thickness of the range shifter plates, the geometrical distance in the patient between these two spots could be completely different (see figure 2.9).

2.5.2.2 The lateral spot scanning distance

For any spot scanning technique the lateral distance between two spot positions is very important. If the distance between two spots is too large a homogenous dose distribution cannot be achieved, but if the distance is too small too many spots are used during the optimization process and during the delivery of the fluence. This unnecessarily increases the compution and delivery time of the treatment plan. The same is also true for the leaf size of the multileaf collimator for photon beams [10].

The lateral dose distribution of a pencil beam for photons and protons can be assumed to be a Gaussian distribution. Bortfeld et al. [10] have found that by using the value of the standard deviation σ as the distance between two sampling points a Gaussian distribution is sampled with an error in the frequency domain of less than 1%. The full width at half maximum (FWHM) of a Gaussian distribution is given by

$$\begin{aligned} \text{FWHM} &= 2\sqrt{2\ln 2}\cdot\sigma && (2.21)\\ &= 2.35482\cdot\sigma. && (2.22) \end{aligned}$$

A good estimate of the resolution of the lateral spot grid in the isocenter plane is therefore given by one third of the FWHM of the particle beam.

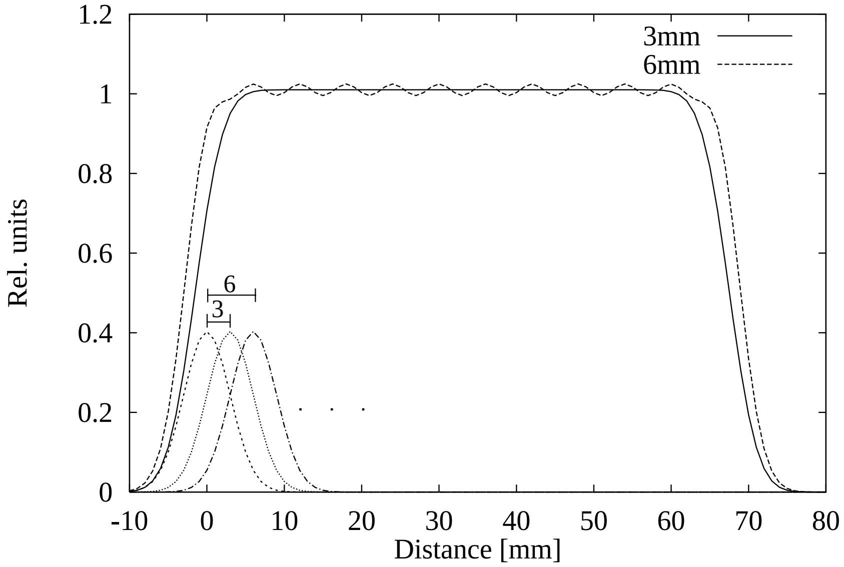

Figure 2.10: *Superposition of multiple Gaussian distributions* $\frac{1}{\sqrt{2\pi\sigma^2}}exp(-\frac{x^2}{2\sigma^2})$ *with standard deviations* σ *of* 3 *mm. The solid line is the result of 22 Gaussian distributions added with a distance of* 3 *mm between each. The dashed lines are the resulting dose distribution for 11 Gaussians with a sampling distance of* 6 *mm.*

The difference between a sampling distance of 3 mm and 6 mm can be seen in figure 2.10. The standard deviation σ of the pencil beam is 3 mm. The solid line is the superposition of 22 Gaussian distributions with a distance of 3 mm. The dashed line shows the result for 11 Gaussians with a distance of 6 mm. The variation between the maximum and minimum value for the dashed line in the range from 30 to 40 mm is approximately 3% where there is no visible variation for the solid line.

Chapter 3

Inclusion of accurate dose calculation algorithms

As already explained in section 2.3, one advantage is the possibility of using more accurate dose calculation algorithms with the D_{ij} matrix method. To test these abilities, a finite pencil beam algorithm for photons and a pencil beam for heavy, charged particles was developed and implemented into the new planning tool. Also an interface to link the treatment planning system with more sophisticated dose calculation algorithms like Monte Carlo techniques or superposition algorithms was created. The modular concept of the new planning tool enables the use of any other dose calculation algorithm.

3.1 Geometrical setup of patient and gantry system

Information about the position of the tumor and the organs at risk inside the patient's body are based on the CT scan. The coordinates of these organs are given in the CT coordinate system ($\vec{p}_{\mathrm{CT}}$). It is a right-handed coordinate system with the origin at the target point. It results from a table rotation around the z axis of the IEC coordinate system. The origin of the IEC system [31, 32] is the isocenter of the treatment room (see figure 3.1(a)).

The third coordinate system is given by the gantry rotation. In the gantry coordinate system the radiation source is located at the position $\vec{p}_{\mathrm{gantry}} = (0, 0, SAD)$ (SAD = source axis distance).

The coordinates of a point given in the CT coordinate system can be transferred into the gantry coordinate system by the following matrix multiplication:

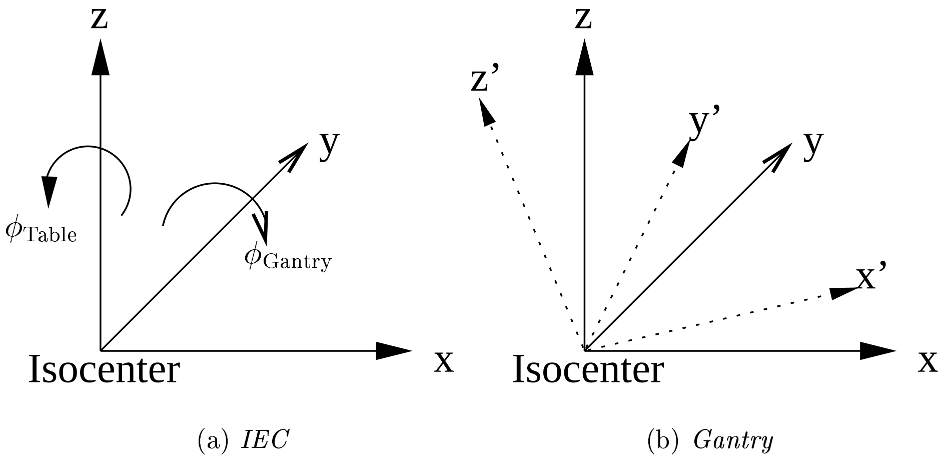

(a) *IEC* (b) *Gantry*

Figure 3.1: *The coordinate systems of the planning tool: (a) IEC coordinate system: The origin of the IEC coordinate system is located at the isocenter of the treatment room. The positive z-axis is upwards towards the ceiling. The positive y-axis points towards the linac. The gantry rotates around the y, the table around the z axis. (b) Gantry coordinate system: The dashed lines represent the gantry coordinate system. The source is located at the positive* z' *axis.*

$$\vec{p}_{\text{gantry}} = \begin{bmatrix} \cos(\phi_{\text{Table}})\cos(\phi_{\text{Gantry}}) & -\sin(\phi_{\text{Table}})\cos(\phi_{\text{Gantry}}) & -\sin(\phi_{\text{Gantry}}) \\ \sin(\phi_{\text{Table}}) & \cos(\phi_{\text{Table}}) & 0 \\ \cos(\phi_{\text{Table}})\sin(\phi_{\text{Gantry}}) & -\sin(\phi_{\text{Table}})\sin(\phi_{\text{Gantry}}) & \cos(\phi_{\text{Gantry}}) \end{bmatrix} \vec{p}_{\text{CT}} \tag{3.1}$$

Another matrix multiplication is necessary to include the collimator rotation into the different coordinate systems.

In figure 3.2 the geometrical setup for all dose calculation algorithms in this thesis is given. $\vec{p}_i$ is the vector from the source to the voxel i, η_i is the radiological depth of the voxel i. d_i is the geometric depth along the central ray. $l_{x,ij}$, $l_{y,ij}$ and $r_{l,ij}$ are the lateral displacements of voxel i measured from the central ray of the bixel j.

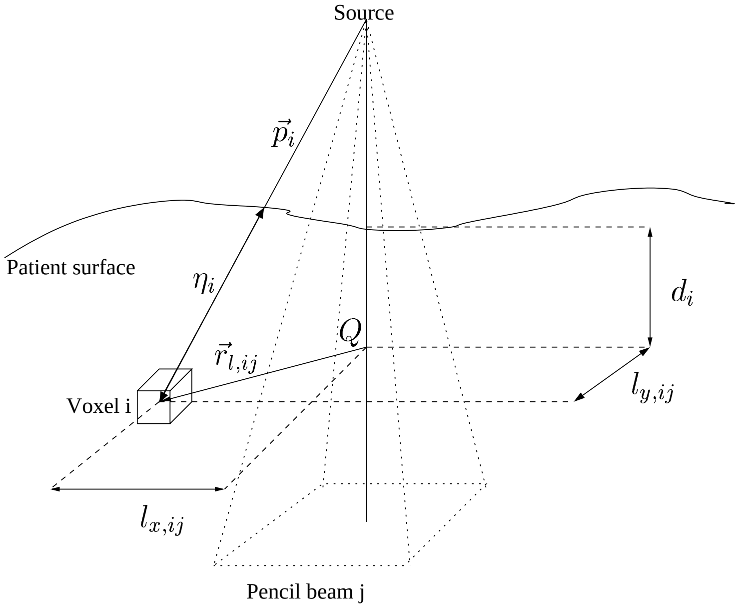

Figure 3.2: *Geometric setup for any dose calculation algorithm.*

3.2 A finite pencil beam dose calculation model

3.2.1 Methods

The aim of the finite pencil beam dose calculation is to calculate the D_{ij} matrix. For every bixel j the dose at any voxel i is calculated and stored in the D_{ij} matrix. Before the dose engine starts the dose calculation, the user has already specified the bixel resolution and the beam energy which should be used for every beam. The finite pencil algorithm relies on precalculated dose distributions. For every bixel resolution used a 3D water-dose distribution in a non-divergent coordinate (fan-line) system must be already available [36]. To calculate these finite pencil beams, any dose calculation algorithm can be used. For the new planning tool a modification of the algorithm by Bortfeld et al. was used [12]. Another advantage of the finite pencil beam approach is that any radiation modality can be optimized with the system if the precalculated finite pencil beams are available for this modality.

3.2.1.1 Stored finite pencil beam

To calculate the 3D dose distribution for the finite pencil beams a water phantom was used together with the DKFZ photon dose calculation module [12]. It is important that the finite pencil beams are stored in the fan-line coordinate system.

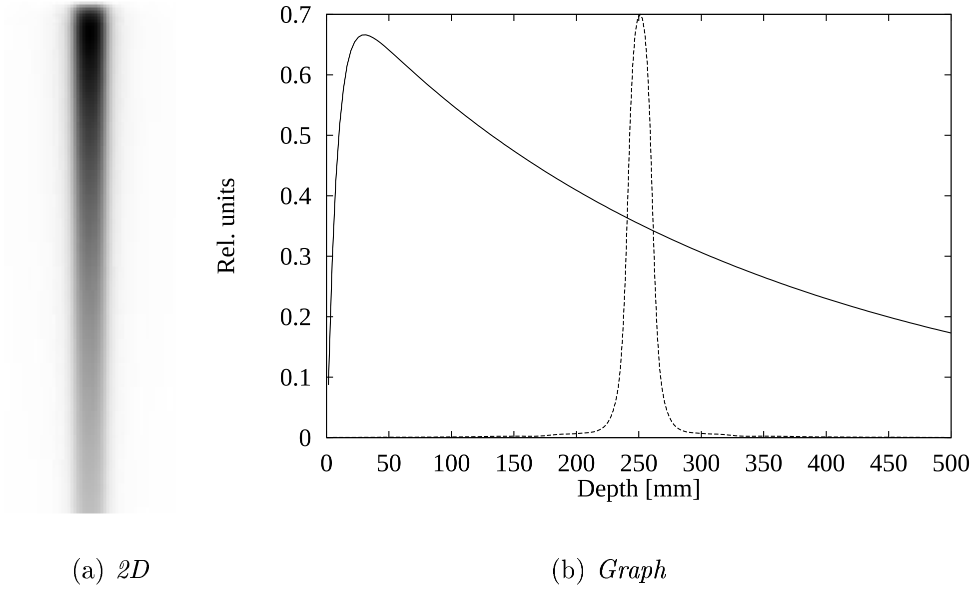

(a) *2D* (b) *Graph*

Figure 3.3: *Finite photon (*15 *MeV) pencil beam dose distribution for a* 10 *mm by* 10 *mm bixel resolution grid (a) Two dimensional view of the dose distribution through the isocenter (b) Depth-dose curve (solid line) and a lateral profile (dashed line) for the depth of* 50 *mm.*

By using the fan-line system only one finite pencil beam must be calculated for any possible source surface distance (SSD). In figure 3.3(a) the two dimensional dose distribution of a finite 15 MeV photon pencil beam is shown.

3.2.1.2 Conversion of Hounsfield units to electron densities

The information given by the patient CT cube is in Hounsfield units (HU) [29]. The Hounsfield units are defined as

$$HU = 1000 \cdot \frac{\mu - \mu_{\mathrm{H_2O}}}{\mu_{\mathrm{H_2O}}}, \tag{3.2}$$

where μ and $\mu_{\mathrm{H_2O}}$ are the photon attenuation coefficients. To include heterogeneity in the dose calculation relative electron densities are needed. A stored table of measured Hounsfield and relative electron densities is used during the conversion. The nonlinearity of the conversion table is due to the Z (atomic charge) dependency of the attenuation coefficient. See figure 3.4 for the current conversion table.

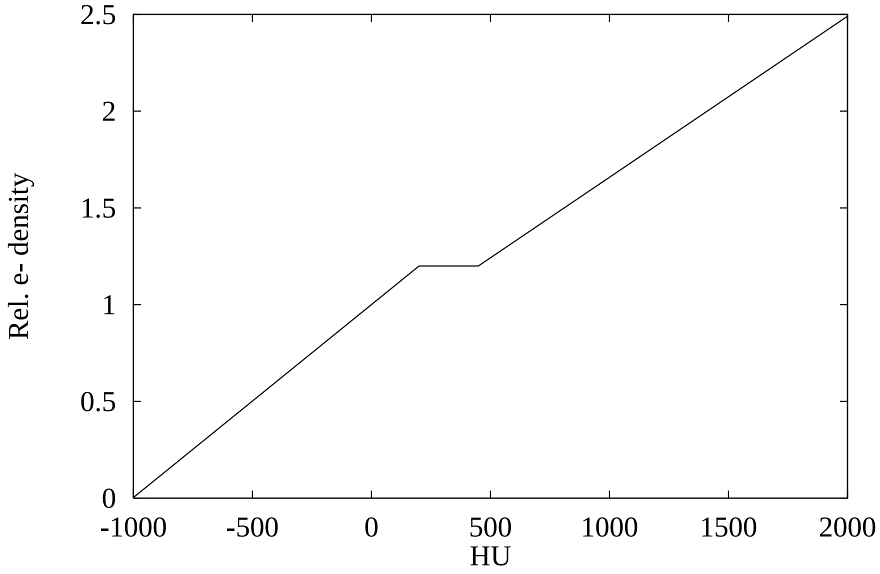

Figure 3.4: *Hounsfield unit (HU) conversion table.*

3.2.1.3 D_{ij} matrix calculation

To calculate the D_{ij} matrix elements for a bixel j the following steps must be performed for each voxel i:

1. Calculate the radiological depth of the voxel i by doing a raytracing in the gantry coordinate system from the source to the voxel i. The radiological depth of the voxel i is then given by

$$\eta_i = \sum_r \rho_r \Delta x_r, \tag{3.3}$$

   where ρ_r is the relative electron density for the voxel r and Δx_r the length of the ray inside the voxel r.

2. Calculate the lateral displacement $l_{x,ij}$ and $l_{y,ij}$. (see figure 3.2)

3. Convert the lateral coordinates of the voxel i from the divergent beam system into the fan-line system

$$l^f_{x,ij} = l_{x,ij}\frac{SAD}{SAD + d_i} \tag{3.4}$$

$$l^f_{y,ij} = l_{y,ij}\frac{SAD}{SAD + d_i}. \tag{3.5}$$

4. Read the value $D_{\mathrm{pb}}(\eta_i, l^f_{x,ij}, l^f_{y,ij})$ from the pre-calculated finite pencil beam by bi-linear interpolation in the stored cube values.

5. Calculate the D_{ij} matrix element

$$D_{ij} = D_{\mathrm{pb}}(\eta_i, l^f_{x,ij}, l^f_{y,ij}) \left[\frac{SAD}{SAD + d_i}\right]^2 f_{\mathrm{c},j}, \tag{3.6}$$

   where $f_{\mathrm{c},j}$ is a correction factor which for example takes into account the primary fluence distribution of the linear accelerator.

These steps must be repeated for every voxel and bixel to create the full D_{ij} matrix.

To save memory and reduce the computational load the methods of a compact matrix storage are used. For example only voxels with a value different from zero are stored in the matrix. See 2.3 for a more detailed explanation of the techniques used.

Any radiation modality where radiological depth scaling can reliably be used to create accurate dose distributions can be optimized with this finite pencil beam model. For example the electron dose distributions in this thesis are calculated this way by using Monte Carlo generated electron finite pencil beams [35].

3.2.2 Comparison with measured data

To check the accuracy of the finite pencil beam algorithm developed different field geometries were calculated and tested against measured water phantom data. In figure 3.5 the results of the comparison for a 15 MeV photon plan for a 3 cm by 3 cm and a 10 cm by 10 cm field, both composed of 10 mm by 10 mm bixels, are shown. The calculated data are in good agreement with the measured data. The comparisons were made in a homogeneous water phantom. For heterogeneous phantoms or patients, a radiological depth scaling is used which is accurate enough for most of the patients. For special cases like lung tumors one should use more sophisticated dose calculation algorithms like Monte Carlo or superpositions during the optimization. These algorithms can handle steep gradients in the Hounsfield values better than pencil beam algorithms. For example the re-buildup effect is not modeled by pencil beam algorithms [66].

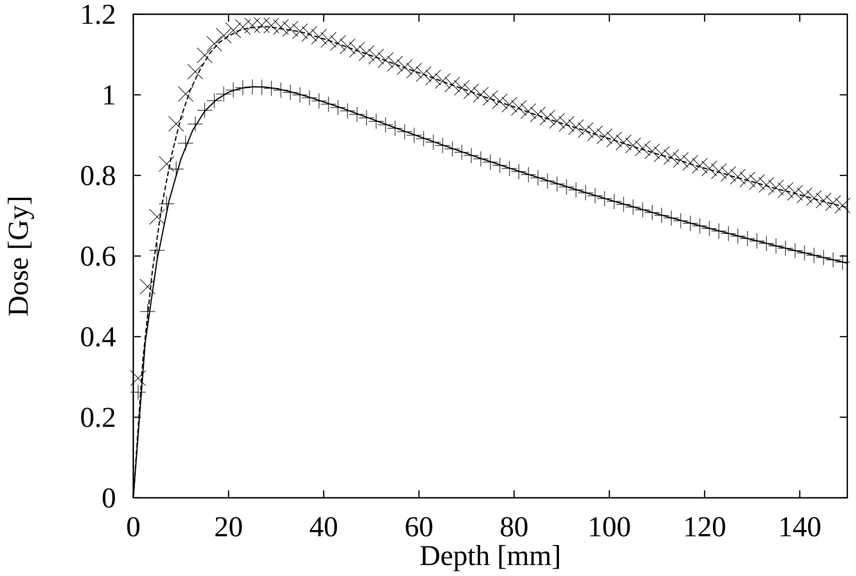

(a) *Depth-dose curve*

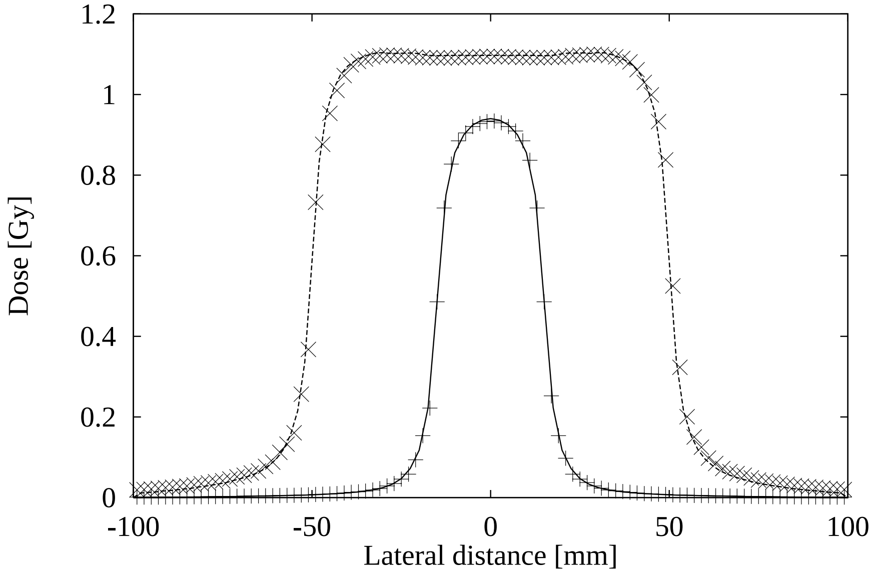

(b) *Lateral profile along x-axis (depth = 50 mm)*

Figure 3.5: *Comparison of measured (cross points) and calculated data for a 15 MeV 3 cm by 3 cm field (solid line) and a 10 cm by 10 cm field (dashed line) photon plan (SSD = 950 mm, 100 monitor units).*

3.3 A proton dose calculation model

3.3.1 Methods

Other import radiation modalities for the treatment of cancer are heavy, charged particles. To date, at least 32000 patients have been treated with heavy, charged particles [69]. The heavy, charged particle pencil beam algorithm developed in this section focuses mostly on protons but can also handle any other heavy, charged particle like carbon or oxygen as well.

The proton pencil beam developed in this thesis has been optimized for spot scanning devices [39, 50, 64]. For broad proton fields there are various pencil beam algorithms available [23, 28, 60].

The geometrical setup for the proton dose calculation is the same as for the finite photon pencil beam. See figure 3.2 for an overview of the variables used.

The proton pencil beam is separated into a central axis and a lateral part. The dose at a point $\vec{p_i}$ with a given radiological depth $\eta(d_i)$ and a lateral distances $l_{x,ij}$ and $l_{y,ij}$ from the central ray of the bixel j is then given by

$$D(\eta(d), l_{x,ij}, l_{y,ij}) = D_{\text{CAX}}(\eta(d_i)) \cdot L(\eta(d_i), l_{x,ij}, l_{y,ij}). \tag{3.7}$$

$D_{\text{CAX}}(\eta(d_i))$ is the central axis (CAX) part of the depth-dose curve. The central dose D_{CAX} only depends on a single parameter, the water depth d. The model developed uses a measured CAX part of a broad proton beam. The measured data is then stored on a non-equidistant grid for later use. The grid resolution is increased near the Bragg peak (the maximum of the depth dose curve) to sample the measured depth-dose curve with a good accuracy. The value for $D_{\text{CAX}}(\eta(d_i))$ is the result of the linear interpolation on a non equidistant grid (see figure 3.6).

By using measured data for the CAX part of the pencil beam the energy straggling and also the energy spectrum of the linear accelerator are taken into account.

The second part $L(\eta(d_i), l_{x,ij}, l_{y,ij})$ describes the off-axis part of the dose distribution. The off-axis part for heavy, charged particles can be approximated by a Gaussian distribution [24] with a depth dependent sigma value:

$$L(\eta(d_i), l_{x,ij}, l_{y,ij}) = \frac{1}{\sqrt{2\pi\sigma_{x'}^2(\eta)}} e^{-\frac{l_{x,ij}^2}{2\sigma_{x'}^2(\eta)}} \frac{1}{\sqrt{2\pi\sigma_{y'}^2(\eta)}} e^{-\frac{l_{y,ij}^2}{2\sigma_{y'}^2(\eta)}} \tag{3.8}$$

$$\sigma_{x'}(\eta) = \sqrt{\sigma_x^2 + \sigma_{\text{MCS}}^2(\eta)} \tag{3.9}$$

$$\sigma_{y'}(\eta) = \sqrt{\sigma_y^2 + \sigma_{\text{MCS}}^2(\eta)}. \tag{3.10}$$

The sigma of the lateral part of the pencil beam is split into two components.

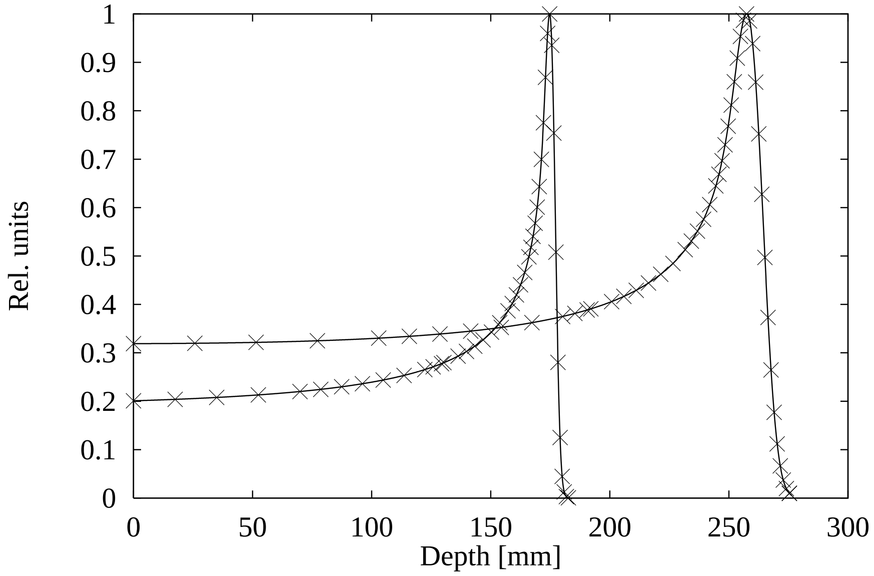

Figure 3.6: *Proton depth-dose curve for a* 160 *MeV (maximum range of* $r_0 = 174.5$ *mm) and* 200 *MeV* ($r_0 = 257.4$ *mm) beam. The solid lines are measured Bragg peaks. The curves are sampled at the positions marked with a cross.*

1. $\sigma_{x,y}$: Due to the finite size of the proton source and the scatter of the primary protons within the nozzle, the proton beam has already a lateral extension before it enters the patient. The values which are used for both sigmas can be obtained by measuring the primary fluence with an ionization chamber in air [64].

2. $\sigma_{\mathrm{MCS}}(d)$: The beam broadening inside the patient is due to the multiple Coulomb scattering of the heavy, charged particles and can be modeled by using a depth dependent sigma value.

The measured values for $\sigma_{x,y}$ are stored in the planning system database. The values for $\sigma_{\mathrm{MCS}}(d)$ are calculated by using the small angle scattering theorem for the multiple Coulomb scattering by Gottschalk et al. [24] and are also stored in the database.

3.3.1.1 Calculation of the multiple Coulomb scattering

To obtain $\sigma_{\mathrm{MCS}}(d)$ we are using the small angle scatter theorem for monoenergetic proton beams by Gottschalk et al. [24],

$$\sigma^2_{\mathrm{MCS}}(z) = \frac{(19.2\mathrm{MeV})^2}{2L_R}(1.0 + 0.088 \log \frac{z}{L_R})^2 I_A \tag{3.11}$$

$$I_A = \int_0^z (z-z')^2 \frac{1}{(p \cdot v(E_0, z))^2} dz', \tag{3.12}$$

where L_R is the mean radiation length, z the depth and E_0 the mean energy of the proton energy spectrum of the beam. This approximation is valid since the energy spectrum has a narrow Gaussian distribution. The mean radiation length [3, 33] for water (O: $Z = 8$ $A = 16$ $w = \frac{16}{18}$, H: $Z = 1$ $A = 1.008$ $w = \frac{2}{18}$) can be calculated by using

$$\rho \cdot L_R = \frac{716.4\mathrm{g\ cm}^{-2} A}{Z(Z+1)\ln(\frac{287}{\sqrt{Z}})} \tag{3.13}$$

$$\frac{1}{L_R} = \sum \frac{w_j}{L_{R,j}} \tag{3.14}$$

$$\frac{1}{L_R} \approx 0.02753 \frac{1}{\mathrm{cm}}. \tag{3.15}$$

Up to the clinically used energies of 260 MeV the nonrelativistic approximation is valid:

$$p \cdot v \approx \frac{p^2}{m_0} = 2T. \tag{3.16}$$

To calculate the kinetic energy of a particle beam the following fit by Bortfeld et al. [8, 11] can be used:

$$T(z) = \frac{1}{\alpha^{\frac{1}{p}}}(r_0 - z)^{\frac{1}{p}}, \tag{3.17}$$

where $\alpha = 2.2 \cdot 10^{-3}\mathrm{cmMeV}^{-p}$, $p = 1.77$, and r_0 is the maximum range of the proton beam for a given energy E_0.

The integral I_A can then be simplified to

$$I_A = \frac{1}{4}\alpha^{\frac{2}{p}} \int_0^z (z-z')^2 \frac{1}{(r_0 - z')^{\frac{2}{p}}} dz' \tag{3.18}$$

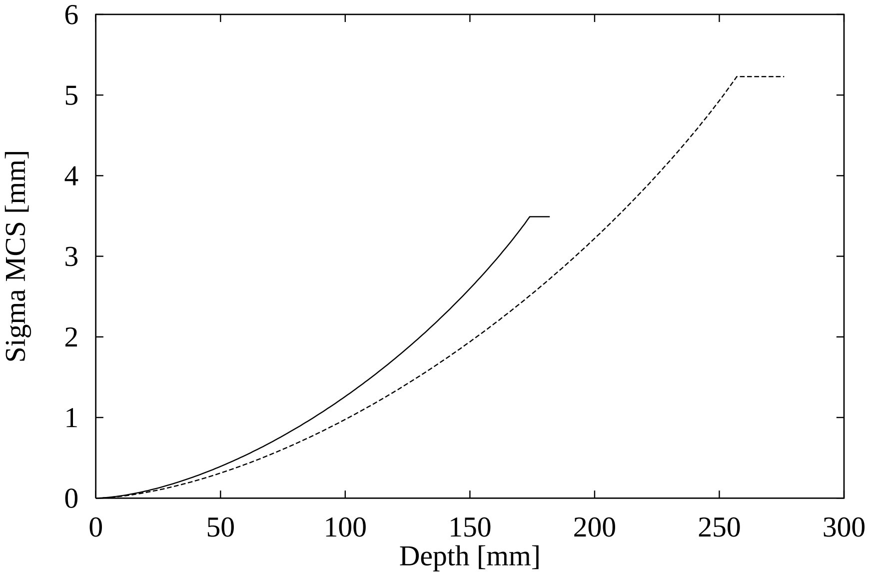

Figure 3.7: *Calculated multiple Coulomb scattering σ_{MCS} for a* 160 *MeV (solid line) and* 200 *MeV (dashed line) proton beam.*

and by using $y = r_o - z'$ the analytical solution yields

$$
\begin{aligned}
\sigma^2_{\mathrm{MCS}}(z) = & \frac{(19.2\mathrm{MeV})^2}{2L_R}(1.0 + 0.088\log\frac{z}{L_R})^2\frac{1}{4}\alpha^{\frac{2}{p}} \\
& \Bigg[(r_0 - z)^2\frac{1}{(1-\frac{2}{p})}(r_0^{1-\frac{2}{p}} - (r_0 - z)^{1-\frac{2}{p}}) \\
& - 2(r_0 - z)\frac{1}{(2-\frac{2}{p})}(r_0^{2-\frac{2}{p}} - (r_0 - z)^{2-\frac{2}{p}}) \\
& + \frac{1}{(3-\frac{2}{p})}(r_0^{3-\frac{2}{p}} - (r_0 - z)^{3-\frac{2}{p}})\Bigg].
\end{aligned}
\tag{3.19}
$$

The values for σ_{MCS} are calculated in a water phantom for every available particle energy. The result is stored in the base data files of the planning system. To handle inhomogeneous phantom data or real patient data the water depth z needs to be replaced with the radiological depth $\eta(z)$ for the calculation point.

Another possible solution for finding the σ_{MCS} values is to feed measured multiple Coulomb scatter data into the planning system.

3.3.1.2 D_{ij} matrix calculation

To calculate the D_{ij} matrix elements for a bixel j the following steps must be carried out for each voxel i:

1. The radiological depth for the point Q is calculated by doing a raytracing in the gantry coordinate system from the source to the point Q (Q is the starting point of vector $\vec{r}_{l,ij}$) (see figure 3.2). The radiological depth of the point Q is then given by

$$\eta(d_i) = \sum_r S_{\mathrm{rel}_r} \Delta x_r, \tag{3.20}$$

   where S_{rel_r} is the relative stopping power [61, 65] for the voxel r and Δx_r the length of the ray inside the voxel r.

2. Calculate the lateral displacement $l_{x,ij}$ and $l_{y,ij}$.

3. Calculate the D_{ij} matrix element

$$\begin{aligned} D_{ij} =& D_{\mathrm{CAX}}(\eta(d_i)) \cdot L(\eta(d_i), l_{x,ij}, l_{y,ij}) & (3.21) \\ =& D_{\mathrm{CAX}}(\eta(d_i)) \cdot \frac{1}{\sqrt{2\pi\sigma_{x'}^2(\eta)}} e^{-\frac{l_{x,ij}^2}{2\sigma_{x'}^2(\eta)}} \frac{1}{\sqrt{2\pi\sigma_{y'}^2(\eta)}} e^{-\frac{l_{y,ij}^2}{2\sigma_{y'}^2(\eta)}}. & (3.22) \end{aligned}$$

These steps must be repeated for every voxel and bixel to calculate the full D_{ij} matrix.

3.3.1.3 Limitation of the pencil beam algorithm

With the appropriate input data, the proton pencil beam algorithm developed can also be used to calculate the physical dose distribution of other heavy, charged particles like carbon or oxygen, but it is not possible to calculate the biological dose since the biological dose contains nonlinear effects. Equation 2.2 must be modified to include biological models but the D_{ij} matrix can be still used. There is no relative biological efficiency (RBE) model [15, 40] in the current implementation of the planning system included.

The range straggling of the particle beams is taken into account for the CAX part of the dose distribution. In the multiple Coulomb scattering calculation there is no correction term for this effect [59]. The effect is very small and can be neglected in the optimization process. If measured data for σ_{MCS} are used, range straggling and the energy spectrum of the beam are automatically taken into account.

In general, pencil beam algorithms cannot fully handle inhomogeneities inside the patient [5]. Schaffner et al. [62] improved the accuracy of the pencil beam dose calculation, but at this time the Monte Carlo (MC) dose calculation is by far the best method for taking inhomogeneity effects into account. One possible way to use Monte Carlo calculations with the new planning tool is the link available to external dose calculation algorithms. The MC code calculates the D_{ij} matrix which is later used during the optimization.

3.3.2 Test of the proton dose calculation model

Due to limited access to a proton accelerator, the results of the dose calculations were compared against analytical solutions or the measured data which was used to generate the pencil beams.

3.3.2.1 Homogeneous water phantom

The first test of a new planning system is the ability to reproduce the measured data for a homogeneous water phantom.

1. Single spot in water:
   To test the dose calculation for the spot scanning system the 3D dose distribution of a single spot was calculated and compared to the input data (see figure 3.8). The voxel resolution for this calculation was 2 mm isotropically. The calculated data is in good agreement with the input data. The Bragg peak position is reproduced within 1 mm. The difference in peak position is due to the finite voxel resolution. This test was performed for all available energies and spot scanning devices. The result of these comparisons were always similar to the results shown in figure 3.8.

2. Square field:
   The above test shows the result for the CAX part of the dose calculation (see figure 3.8). To test the lateral part, a 50 mm by 50 mm field was calculated. The distance between the proton spots in both scanning directions was set to 2 mm. To test the multiple Coulomb scattering, lateral profiles at three different depths were compared against the analytical solution for the given sigmas. The CAX part was compared again, too.

   The analytical solution for the lateral profiles is the convolution of a rectangular fluence $\Phi(x)$ with a Gaussian distribution $g(x, \sigma)$:

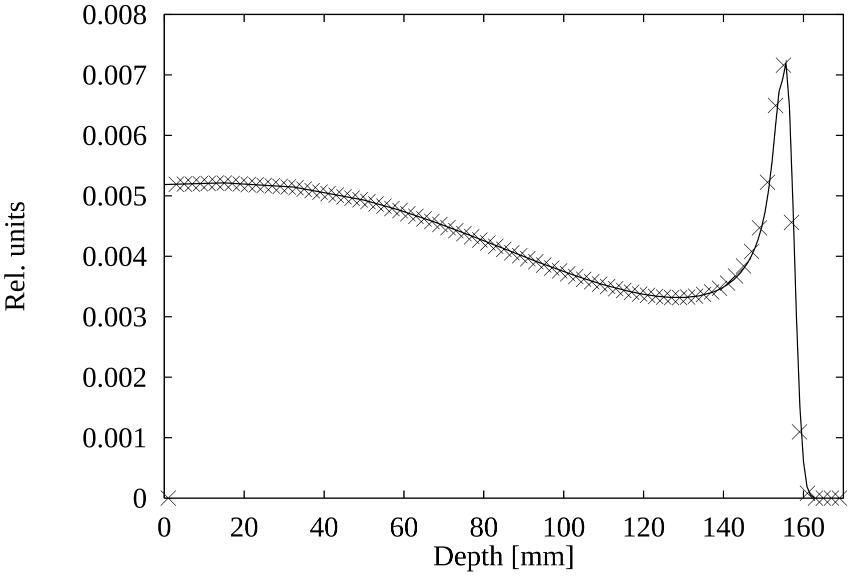

Figure 3.8: *Calculated (cross points) and measured (solid line) depth-dose curve of single* 160 *MeV proton spot (Range shifter was set to* 20 *mm).*

depth [mm]	σ [mm]
70	2.67
120	3.34
170	4.64

Table 3.1: *Calculated σ values for different depths of a* 160 *MeV proton beam*

$$\Phi(x,a) = \begin{cases} 1 & x \leq |\frac{a}{2}| \\ 0 & \text{else} \end{cases} \tag{3.23}$$

$$g(x,\sigma) = \frac{1}{\sqrt{2\pi\sigma^2}} e^{-\frac{x^2}{2\sigma^2}} \tag{3.24}$$

$$\hat{\Phi}(x,a) = \Phi(x,a) * g(x) \tag{3.25}$$

$$= \frac{1}{2}[-\mathrm{erf}(\frac{1}{2\sqrt{2}}\frac{(2x-a)}{\sigma}) + \mathrm{erf}(\frac{1}{2\sqrt{2}}\frac{(2x+a)}{\sigma})]. \tag{3.26}$$

To compare the analytically expected and calculated lateral profiles in different depths the σ values in table 3.1 are used.

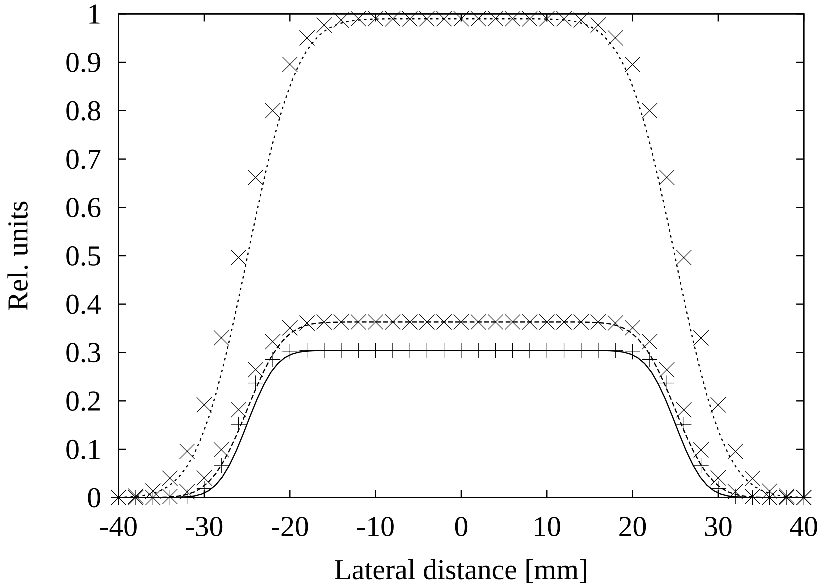

Figure 3.9: *Comparison of calculated and analytically predicted lateral x profiles for a* 160 *MeV proton beam (Range shifter was set to* 20 *mm). (*$d = 70$ *mm bottom,* $d = 120$ *mm middle,* $d = 170$ *mm top) The cross points are the calculated values. Analytical data were normalized to the calculated value on the central axis.*

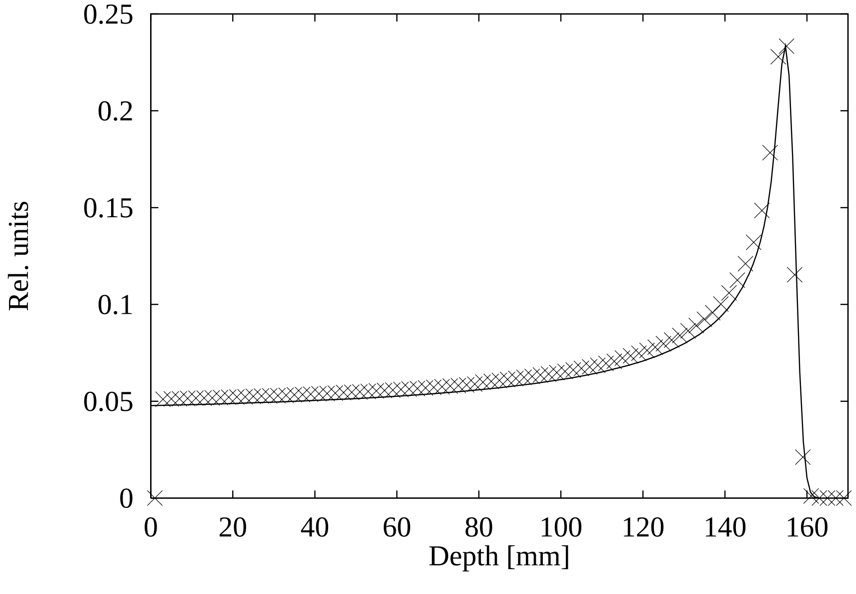

Figure 3.10: *Comparison of the calculated depth-dose curve for a* 50 *mm by* 50 *mm field of a scanning device and the measured depth-dose curve of a broad beam field (*160 *MeV proton beam, range shifter was set to* 20 *mm). The cross points represents the calculated values.*

The result of the comparison between the analytical solution and the values calculated with the proton pencil beam algorithm are shown in figure 3.9. The calculated profiles are always larger than the analytical solutions. This is due to the discrete sampling of the rectangular fluence distribution $\Phi(x)$ with a sampling distance of 2 mm. If the lateral scanner distance between the spots would be reduced to zero both graphs would match exactly. Nevertheless the shape of the gradient is reproduced with great accuracy.

The CAX part of the 50 mm by 50 mm field is compared with the depth-dose curve for a broad beam field. The results in figure 3.10 show that the calculated depth-dose curve is always higher than the measured data. This effect can be explained through the different application modes. The measured depth-dose curve is measured in a broad proton beam while the calculated depth-dose curve is the result of the superposition of 676 proton pencil beams. If the distance between the beam spots is reduced to zero, the depth-dose curve would fit the measured data.

3.3.2.2 Inhomogeneous phantom

As outlined in section 3.3.1.3, there are some minor limitations to the pencil beam model. One of these limitations is the inability to handle inhomogeneous structures inside the patient correctly. To demonstrate this topic, a 2 cm thick slab with the relative stopping power of $S_{\mathrm{rel}} = 1.8$ was placed at a position 6 cm beneath the water surface (see figure 3.11(a)). A single pencil beam with the scanner coordinates of (0,0) is then calculated in the phantom. A transverse slice (figure 3.11(b) of the resulting dose distribution shows the typical isodoses for a single Bragg peak spot (see also figure 3.8). The pencil beam algorithm totally ignores the slab. If the same situation is calculated using a MC dose algorithm [62], a second Bragg peak would be visible at a more proximal position in the dose cube.

The situation in the simulated phantom is an extreme situation. The normal handling of inhomogeneities in the patient by the pencil beam algorithm is accurate enough for most of the patients. Only for tumors with a location near a lot of cavities should the results of the planning tool be recalculated with an external MC algorithm. The preferred solution, as already stressed, is to link the MC algorithm to the planning system by using the D_{ij} matrix approach. To calculate the D_{ij} with MC for protons is a very time consuming process [72] and not available at the DKFZ at present.

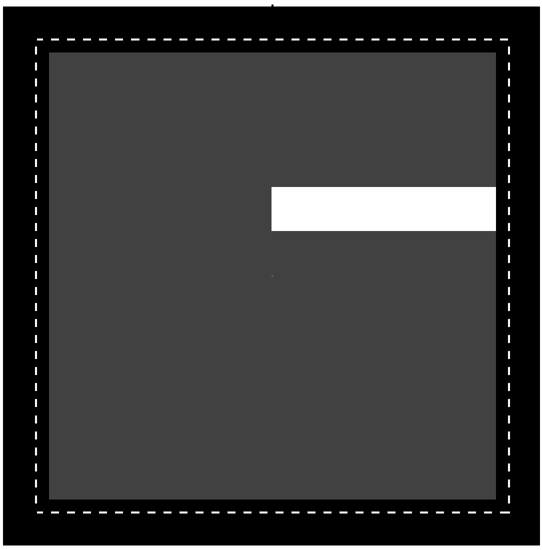

(a) *Transverse CT slice*

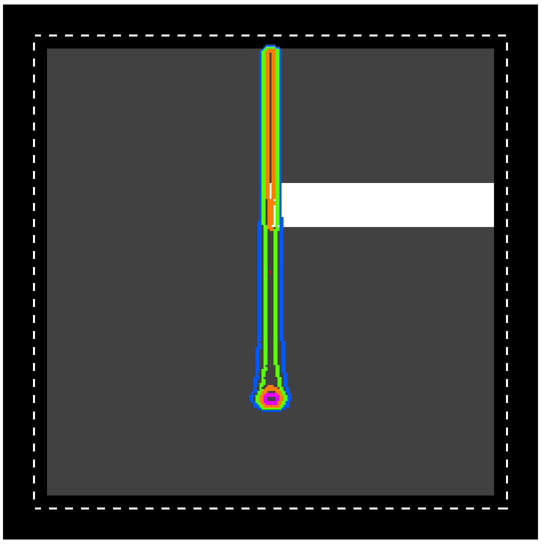

(b) *Relative dose distribution*

Figure 3.11: *2D dose distribution of a* 160 *MeV single proton spot with scanner coordinates (0,0): (a) CT slice of the water phantom with a* 2 *cm slab with the relative stopping power of 1.8 starting at* 6 *cm from the water surface (b) 2D dose distribution calculated with the pencil beam algorithm.*

Chapter 4

Results

4.1 Clinical example cases

In this section the newly developed IMRT planning tool is used to investigate the potential possibilities of IMRT for a number of different radiation modalities. To investigate the clinical applicability of the new system, two representative patients were selected.

The first patient has a clivus chordoma in the head which is located near the brainstem. The target is shaped like a horseshoe. This shape is a typical geometric form which can be best treated by using the IMRT technique to spare the brainstem. Figure 4.1(a) shows a transverse CT slice located at the isocenter. For the optimization of all treatment plans the organ parameters listed in table 4.1 were used. No minimum dose is specified for the organs at risk (OAR). The unassigned tissues within the patient contour are given a maximum dose limit. This procedure results in a better dose gradient at target edges where no OAR is located next to the target volume.

The second patient is a prostate patient. A transverse CT slice and a three dimensional picture of the tumor location (visualized with VIRTUOS [4]) is given in figure 4.2. The problem for the treatment of prostate patients is the proximity of two critical structures (rectum, bladder) adjacent to the prostate target volume. Another problem is the movement of prostate, bladder, and rectum. The position during the treatment therefore changes from day to day. This has to be taken into account during the evaluation of the resulting treatment plans. In addition a boost volume was defined inside the target volume (see figure 4.2(a)). In table 4.2 the organ parameters for the optimization process are listed.

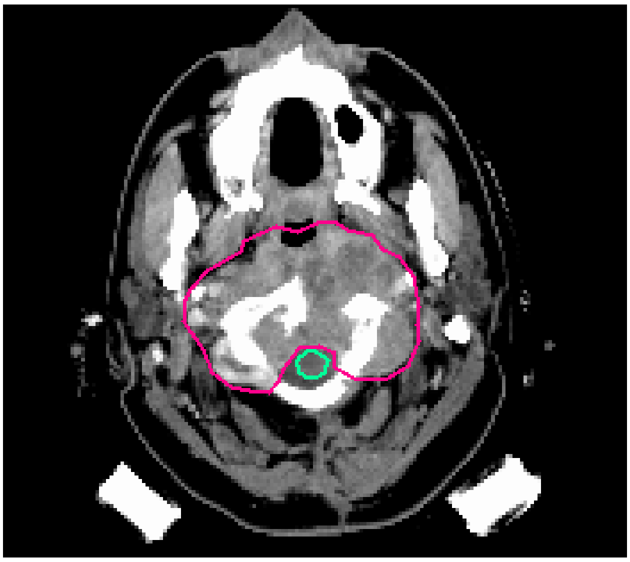

(a) *CT slice*

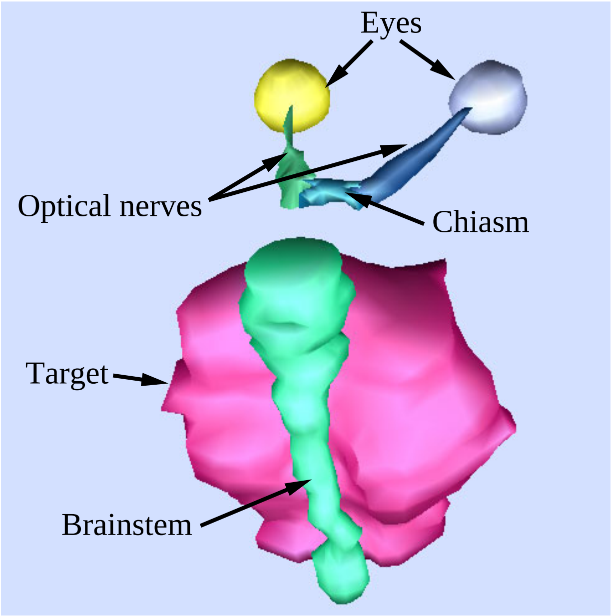

(b) *Observers view*

Figure 4.1: *Clivus chordoma patient: (a) Transverse CT slice through the isocenter. The red line outlines the target and the green line delineates the location of the brainstem. (b) Three dimensional view of the tumor and the different organs at risk.*

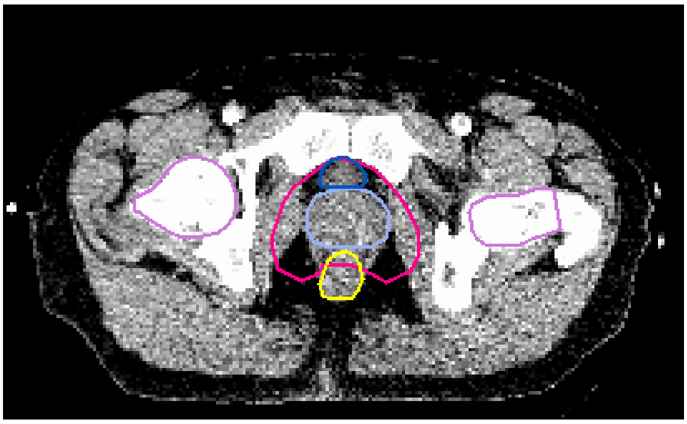

(a) *CT slice*

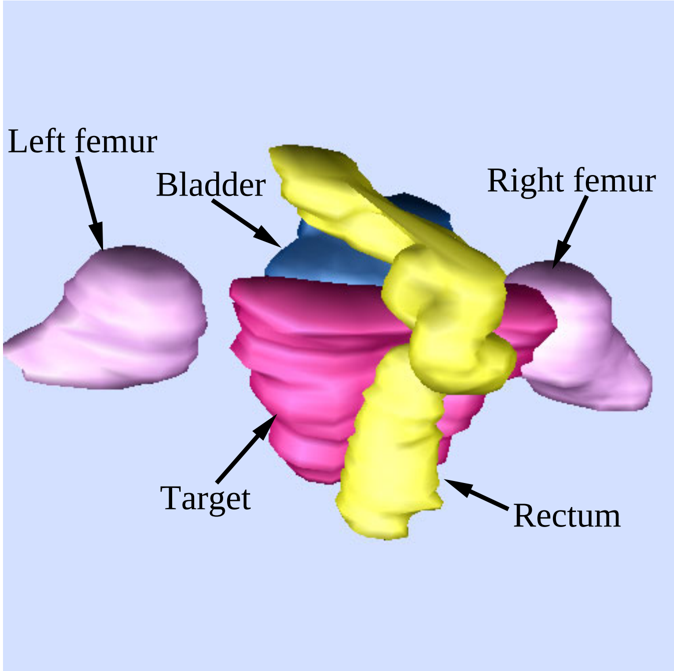

(b) *Observers view*

Figure 4.2: *Prostate patient: (a) Transverse CT slice through the isocenter. The red line outlines the target and the light blue solid line the boost volume. (b) Three dimensional view of the tumor and the different organs at risk. The boost volume is hidden inside the target volume.*

Organ/Tissue	Max Dose [Gy]	Penalty	Min Dose [Gy]	Penalty	Volume [ccm]
Target	71.5	20	68.0	99	203.6
Brainstem	0.0	6	-	-	24.9
Chiasm	60.0	3	-	-	0.9
Left Eye	30.0	3	-	-	5.7
Right Eye	30.0	3	-	-	5.9
Left optic nerve	40.0	3	-	-	0.7
Right optic nerve	60.0	3	-	-	1.2
Pat. contour	70.0	3	-	-	4575.4

Table 4.1: *Organ parameters used during the optimization for the clivus chordoma patient.*

Organ/Tissue	Max Dose [Gy]	Penalty	Min Dose [Gy]	Penalty	Volume [ccm]
Target	66.0	6	66.0	8	286.4
Boost	72.0	4	72.0	8	48.3
Bladder	45.0	4	-	-	108.2
Rectum	45.0	4	-	-	121.5
Left femur	30.0	2	-	-	67.4
Right femur	30.0	2	-	-	75.1
Pat. contour	35.0	3	-	-	7199.1

Table 4.2: *Organ parameters used during the optimization for the prostate patient.*

4.2 Verification of spot positioning algorithm for DET and 3D

In section 2.5.2.1 the algorithm to find the correct spot positions was explained. To verify the algorithm, the spot positions calculated by the planning tool were marked with crosses in the transverse CT slice for the prostate patient.

For the DET technique the particle spots are placed only at the distal edge of the target volume. In figure 4.3(a) the spot positions for a gantry angle of zero degrees

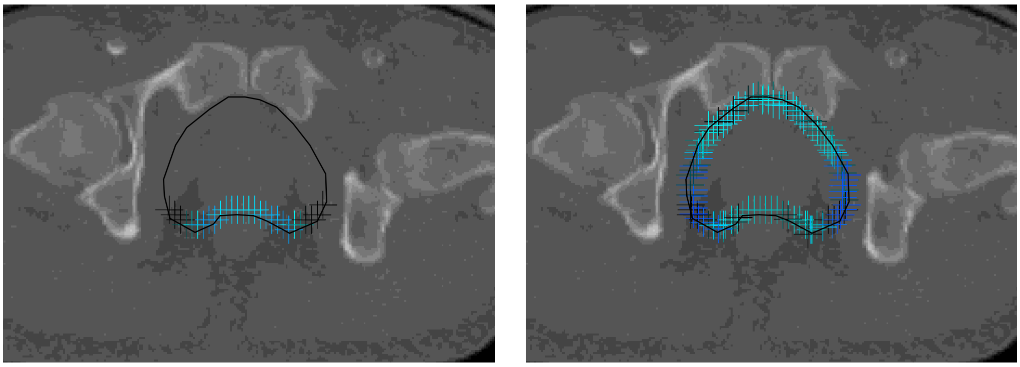

(a) *DET* $\phi_{Gantry} = 0°$ (b) *DET seven beams*

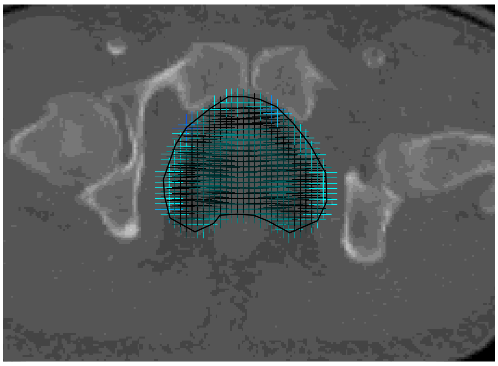

(c) *3D* $\phi_{Gantry} = 0°$

Figure 4.3: *Prostate patient: Verification of beam spot positioning: The black solid line shows the target volume. Black spots have a low weight, blue spots a higher weight. (a+b) Beam spots are positioned right at the edge of the target volume. (c) Beam spots are placed all over the target.*

is given. The spots are always within 1 mm of the desired positions. The beam spots for a seven equidistant, coplanar plan are displayed in figure 4.3(b). The calculated beam spots are in very good agreement with the required placement.

The spot positions in figure 4.3(c) are the result of a 3D technique with a gantry angle of zero. As already mentioned in figure 2.9, the spot positions are calculated not only for the edge of the target volume but also for spot positions inside the target. The distance for the spots in beam direction was set to 3 mm. The distal and proximal positions are within 1 mm of the predicted positions.

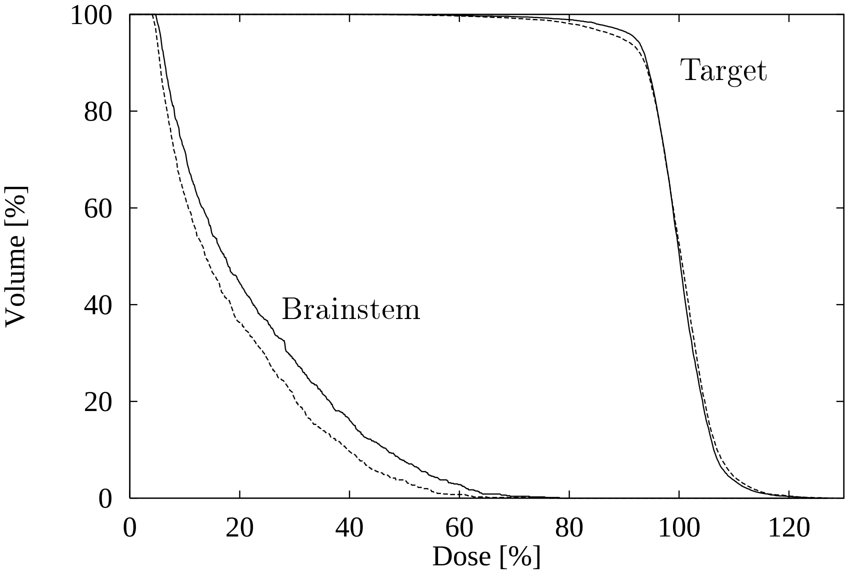

Figure 4.4: *Clivus chordoma: Dose-volume histogram of a seven-beam photon IMRT plan optimized with the integrated (solid line) and the modular (dashed line) optimization loop.*

4.3 Comparison of integrated and modular optimization loop

As already explained in section 2.4.1.3, the use of the D_{ij} matrix approach in combination with accurate dose calculation eliminates the problem of the scatter calculation. For the integrated optimization loop the lateral scatter is only taken into account during the calculation of the 3D dose distribution based on the current fluence distribution, but not during the update of the fluence results. To demonstrate the difference between the two optimization loops the clivus chordoma case was optimized with the same organ parameters (see table 4.1) and the same dose resolution grid in both systems. For both plans the dose distributions are recalculated based on the optimized fluence matrices with the routine planning dose algorithm [12].

Table 4.3 shows an increased minimum target dose for the modular loop. Also the maximum brainstem dose is reduced for the modular loop by 2.1%. The dose-volume histogram for the integrated loop shows a steeper gradient for the target volume but a higher dose-volume histograms (DVH) for the brainstem in all dose levels. This is due to the neglected scatter contribution. Since the brainstem is located right next to the target (see figure 4.1(b)) a significant amount of the

	integrated loop	modular loop
Target: Minimum dose [%]	39.4	42.1
Target: Maximum dose [%]	125.7	123.9
Brainstem: Maximum dose [%]	78.7	76.6

Table 4.3: *Clivus chordoma: Comparison of a seven-beam photon IMRT plan optimized with the integrated and the modular loop. Both plans are normalized to the median target value.*

dose delivered to the brainstem is due to scattered radiation from the target. The integrated loop ignores the contribution of the scatter during the update of the fluence distribution and therefore the brainstem can not be optimally spared. The better sparing of the organs at risk leads to a less steep target DVH for the modular loop optimization.

4.4 Comparison of dose distributions for different radiation modalities

One of the new features of the planning system developed is the ability to optimize different radiation modalities within the same system. It is therefore possible to use the same dose calculation grid resolution and the same optimization algorithm for all modalities. To achieve a good comparison, the same organ parameters are always used.

For this comparison a photon (IMXT), electron (MERT), carbon and proton (IMPT) intensity-modulated treatment plan were calculated for the clivus chordoma patient. The organ parameters listed in table 4.1 were used for all plans. A seven equidistant, coplanar beam setup was chosen. The voxel resolution was set to 2.62 mm in all directions. The result of the photon IMRT plan is used as the reference standard. For the photon and electron plan the bixel resolution was set to 10 mm by 10 mm. The particle treatment plans were optimized with the distal edge tracking technique. The beam spots were placed on a 3 mm lateral grid. The proton scanning device has a $\sigma_{x,y}$ of 2.5 mm. For the carbon treatment device $\sigma_{x,y}$ was set to 3 mm.

Table 4.4 lists the computational values of the different plans. The number of bixels for the photon and electron plans are an order of magnitude smaller than for the particles, but the time for the optimization is roughly the same for all plans. This is due to the number of elements required in the D_{ij} matrix for each

	Photon	Electron	Proton	Carbon
Bixels	496	496	3841	3841
Mean number of voxels per bixel	200000	51000	2500	2000
Number of iterative steps	82	164	231	192
Computer time [s]	567	657	518	466
Computer memory [MB]	595	152	58	51

Table 4.4: *Clivus chordoma: Comparison of the computational parameters for different radiation modalities. All plans were calculated on a Digital Alpha 600 MHz workstation.*

bixel. The number of voxels which receive a significant amount of dose from each bixel is at least a factor of 10 larger for the IMXT and MERT plan than for the IMPT plans. The lateral cutoff for heavy, charged particles is set to three sigma during the calculation of the D_{ij} matrix elements. With a mean sigma for protons of about 5 mm, only voxels within 15 mm are taken into account during the calculation. For the photon dose calculation the lateral cutoff L_c was set to 82 mm. This value is due to the large lateral tail in the photon dose distribution for a 10 mm by 10 mm bixel (see figure 3.3). The superposition of the dose distributions of many bixels must result in the same 3D dose distribution as the calculation of the composite field with a conventional pencil beam algorithm. If the lateral cutoff value is set too small, the dose distributions are not the same, since the dose contributions to voxels from bixels further away than the lateral cutoff value are omitted. If too many bixels are neglected for one voxel the absolute dose for this voxel is therefore reduced significantly compared with the pencil beam dose calculation. For the selected L_c, the maximum possible differences in the absolute dose is 4% but for all practical cases the error is below 2%. For the electron dose calculations L_c was set to 46 mm.

The minimum and maximum doses inside the target are the criteria defined by ICRU 50 [30] for comparing different plans with each other. In table 4.5 the results are listed. The objective values for each plan and the maximum doses for the brainstem are also given. The minimum target dose is very low for all IMRT plans. This is due to the maximum dose constraints of 0 Gy set for the brainstem (see table 4.1). The brainstem is located next to the target volume and there is a physical limitation to the possible gradient which can be achieved with IMRT due to the lateral extension of the pencil beams. The plan with the best value for the minimum dose is the carbon IMRT plan. This plan is even better than the proton plan. Because of the higher mass of the carbon ion, the

	Photon	Electron	Proton	Carbon
Objective value	4120	6878	1535	962
Target: Minimum dose [%]	42.1	51.5	49.6	62.2
Target: Maximum dose [%]	123.9	121.1	121.0	127.0
Brainstem: Maximum dose [%]	76.6	70.9	65.3	57.1
Total dose: [a. u.]	1.0	1.003	0.438	0.428

Table 4.5: *Clivus chordoma: Comparison of different radiation modalities. The objective value, the minimum and maximum dose for the target and the brainstem are listed.*

multiple Coulomb scattering is very small inside the patient which results in a sharper lateral fall-off. Another positive effect is the very sharp Bragg peak of the carbon depth-dose distribution. The maximum dose for the brainstem is reduced significantly by using heavy, charged particles instead of photons. The colorwash dose distribution for all plans in figure 4.5 shows another benefit of heavy, charged particles. The total dose delivered to the patient's body is reduced at least by 56.2%. For carbon ions the total reduction is even higher because of the smaller sigma value.

4.4.1 Comparison of photon and proton plans

Since the majority of the patients are treated with photons and also a large number with protons, a more detailed comparison of these two radiation modalities was performed.

The comparison of the dose-volume histograms (see figure 4.6) of the photon and proton DET IMRT plans shows that, in this case, the coverage of the target is better for the IMPT plan than the IMXT plan. By using charged particles with the physical advantage of a well defined range, better sparing of the brainstem is possible. The maximum dose to the brainstem is reduced from 76.6% for the IMXT plan to 65.3% for the IMPT plan. Also the median dose of the brainstem is reduced by a factor of 5.

Another important advantage of heavy, charged particles is the reduction of the integral dose delivered to the patient. The use of IMRT decreases the dose delivered to the OAR and therefore slightly increases the dose in the normal body tissue. By using heavy, charged particles, the low dose region and the total dose is reduced by at least a factor of two. The mean integral dose to the normal tissue

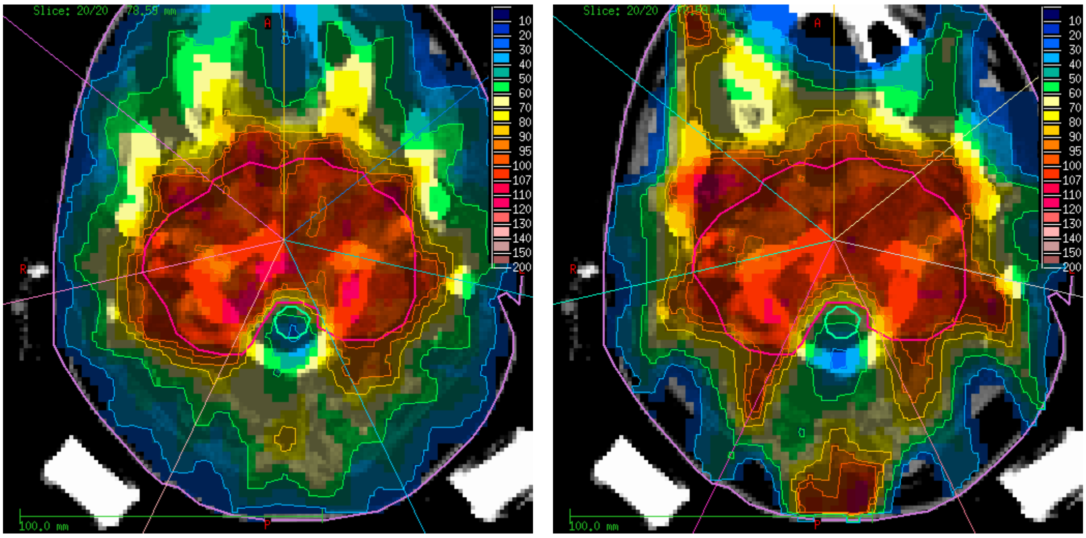

(a) *Photon* (b) *Electron*

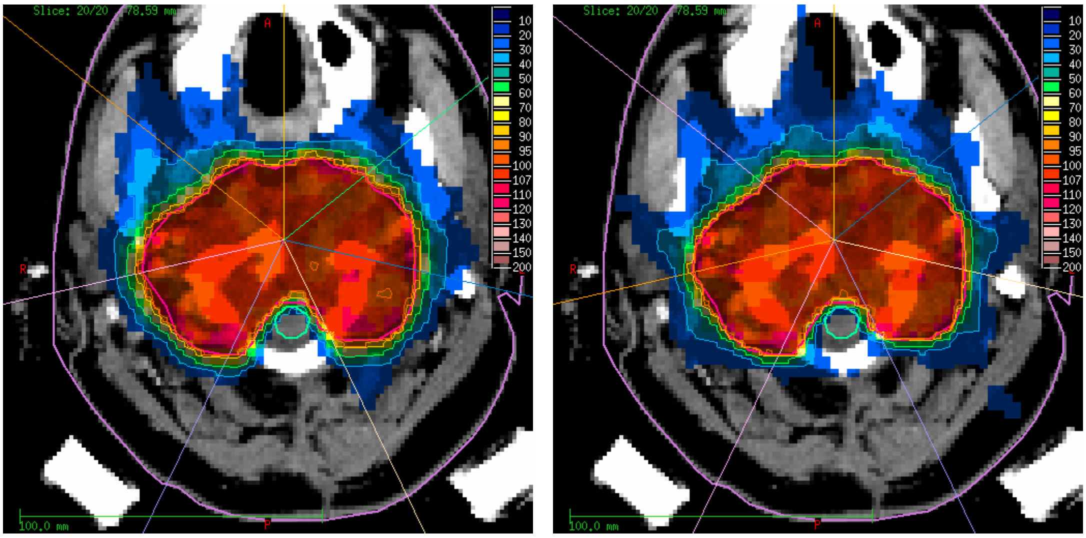

(c) *Proton* (d) *Carbon*

Figure 4.5: *Clivus chordoma: Dose distributions of four radiation modalities. The dose distributions are normalized to median target dose (100%).*

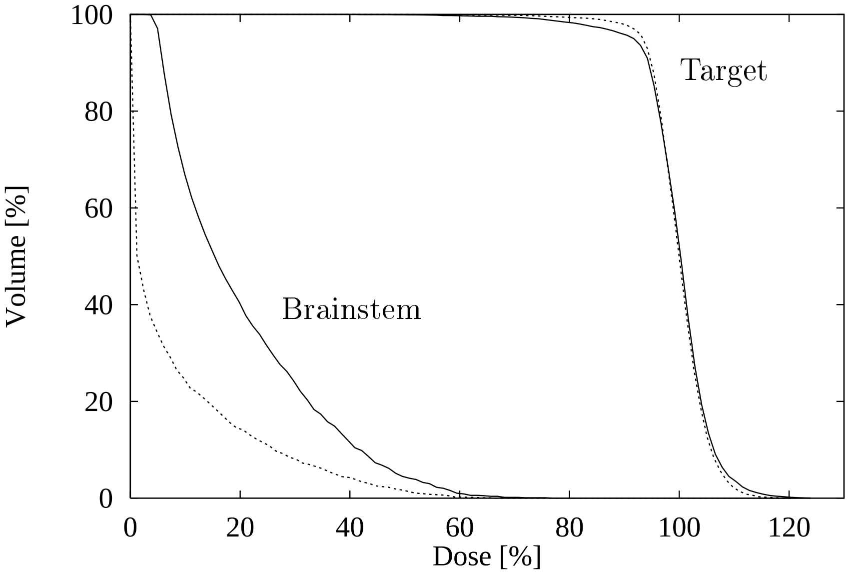

Figure 4.6: *Clivus chordoma: Dose-volume histogram of a seven-beam photon IMRT (solid line) and a seven-beam proton DET IMRT plan (dashed line).*

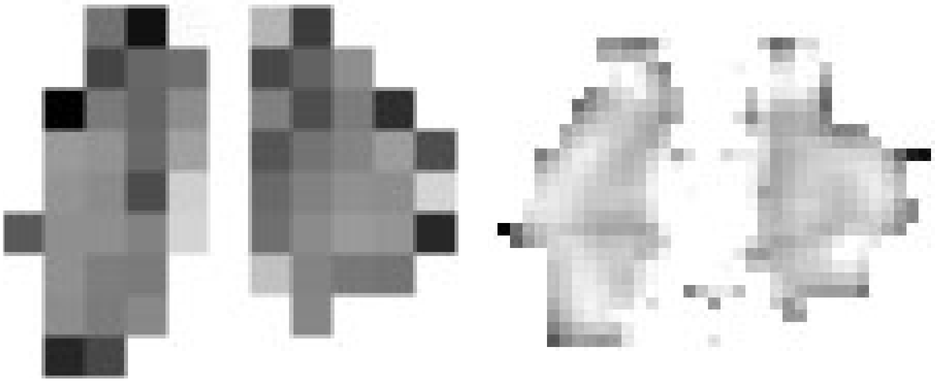

(a) *Photon*

(b) *Proton*

Figure 4.7: *Clivus chordoma: Fluence maps for* $\phi_{Gantry} = 0^\circ$*. Graphic normalized to maximum fluence level (black). The bixel resolution was set to (a)* 10 *mm by* 10 *mm (b)* 3 *mm by* 3 *mm.*

is an important factor for the radiation-induced second malignancies, especially for children [58].

The fluence levels created by the treatment planning system for $\phi_{\text{Gantry}} = 0^\circ$ of the photon and proton IMRT plans are displayed in figure 4.7. The size of the rectangular fields is representative of the size of the fluence bixels. The output of the optimization algorithm for fluence bixels which would irradiate the brainstem directly is almost zero for both plans to fulfill the organ criteria set by the user.

Other comparisons of IMXT and IMPT [19, 52] were done using different optimization and planning tools. By using the same organ parameters and dose calculation grid, the objective value of the different plans can be really used as a measurement of the plan quality. The objective value for the proton plan is 63% of the photon IMRT plan value. (see table 4.4).

The results of the comparison between the proton and photon IMRT plan of the clivus chordoma patient, especially the reduced integral dose and the sparing of the organs at risk for the IMPT plan, were also found for the case of the prostate patient.

4.5 Potential of the DET and 3D technique for protons

As already outlined in section 2.5.2, there are two promising delivery techniques for heavy, charged particles. The new planning system is capable of using both techniques. First the DET and 3D technique are compared based on the clivus chordoma patient. Second the effect of organ motion on the resulting dose distribution is analyzed. For the second study the prostate patient is used, because organ motion in the head can be neglected, but not for the rectum and the bladder. Finally the uncertainties introduced through the spot scanning system and the CT scanner are studied.

4.5.1 Comparison of DET and 3D technique

To explore the potential of both techniques, treatment plans for the clivus chordoma patient with same organ constraints but different numbers of beams were calculated and compared with the help of the dose-volume histograms. For all calculations, the same base data and dose resolution grid were used. The reference standard for all plans is the seven-beam photon IMRT plan.

Table 4.6 provides characteristic values for eight plans. The number of spots (and therefore the calculation time) is always at least a factor ten smaller for the DET technique than for the 3D technique. This is not only important for the planning process but also for the later delivery of the calculated fluence matrices. More

Technique	DET	3D	DET	3D	DET	3D	3D	3D
Beam	7	7	5	5	3	3	2	1
Bixel / Spots	3841	56211	2740	40126	1663	24047	16303	7848
Steps	231	259	214	242	141	240	268	256
Calc. time [s]	518	9229	383	6767	221	4286	3397	1762
Objective value	1535	1630	2239	1723	4327	1805	2396	2335
Min. target [%]	49.6	43.6	49.0	45.8	49.0	44.2	41.9	43.4
Max. target [%]	120.0	121.2	122.3	120.5	143.8	122.5	119.7	124.1
Max. brainstem [%]	65.3	65.4	66.0	67.5	79.1	71.0	69.4	67.0
Total dose [a. u.]	1.0	1.23	0.99	1.23	1.13	1.27	1.19	1.38

Table 4.6: *Clivus chordoma: Comparison of different proton plans calculated with the DET or 3D technique.*

spots increase the treatment time for the patient and therefore the intrafraction movement (movement of the patient during the treatment) is more critical. From this point of view the distal edge tracking technique is always superior to the 3D one.

Given the criteria defined in the ICRU 50 the best plan for the DET technique is the seven-beam plan. One could also choose the five-field DET plan. The plan only differs in the objective value by more than 2%. All other values are comparable with the seven DET plan. The best 3D plan is also the seven-field plan. The three-field plan is a good alternative to the seven-field plan. The number of spots are reduced by a factor of 2.33 by using the three-field plan.

The DVH (see figure 4.8) confirms the selection of the two plans. The target dose-volume histogram of the photon plan has a slightly better gradient than the five-field DET plan. The minimum dose of the target volume is 49.0% for the proton plan but only 42.1% for the photon plan (see figure 4.8(a)).

The DVH for the three beam 3D technique plan is always superior to the photon plan (see figure 4.8(b)).

In conclusion the DET treatment technique in comparison to the 3D technique provides the same quality with only a fraction of the number of spots. The only disadvantage of the DET plans are the higher number of beam directions. But, as shown by the study, the number of beams can be reduced at least to five. Five beams could be delivered with modern gantries within reasonable times.

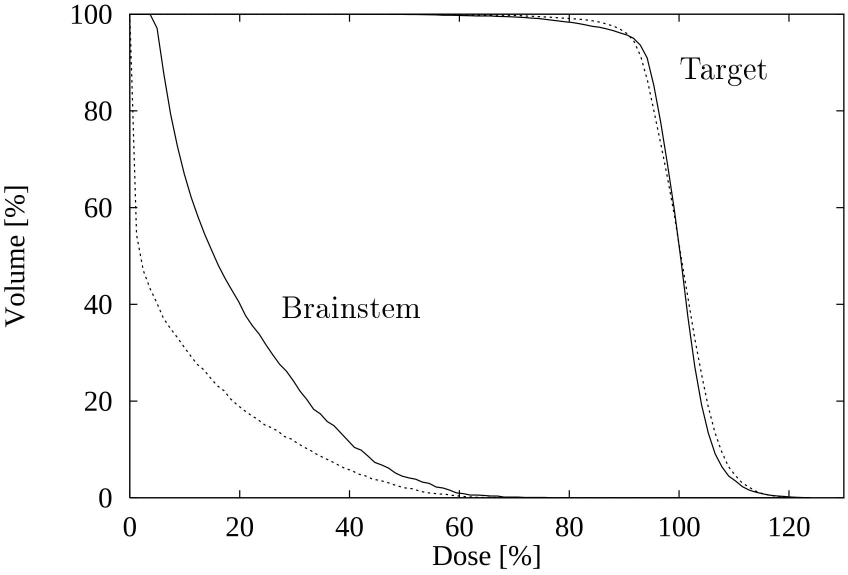

(a) *Photon versus DET 5 beams*

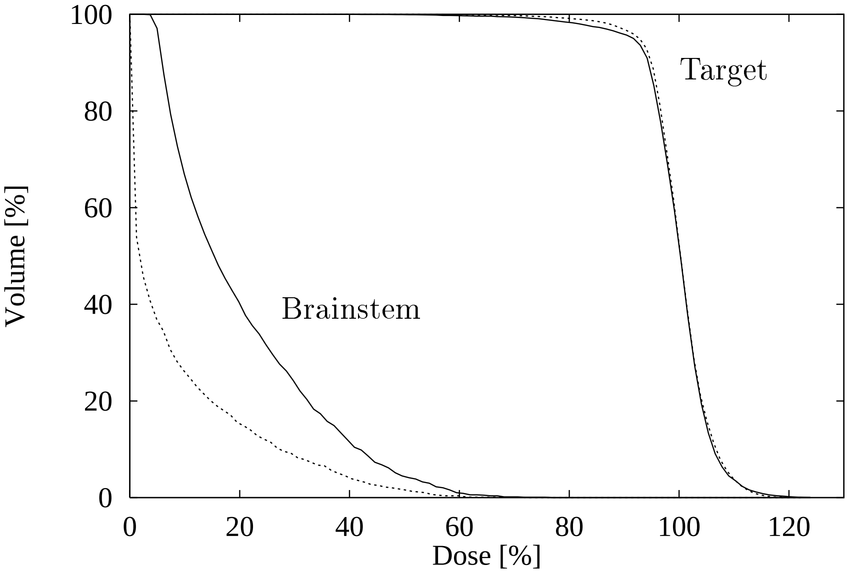

(b) *Photon versus 3D 3 beams*

Figure 4.8: *Clivus chordoma: Comparison of a seven-beam photon IMRT plan (solid line) and (a) five-beam DET technique plan and (b) a three-field 3D technique plan (dashed line).*

Radiation	Minimum Dose [%]			Maximum Dose [%]		
	TM	Target	TP	TM	Target	TP
Photon	69.5	73.9	70.6	110.3	110.3	110.3
DET	54.7	72.2	52.5	109.4	109.4	109.4
3D	52.0	71.3	55.4	113.2	113.2	113.2

Table 4.7: *Prostate: Comparison on the effect of organ motion for different radiation modalities.*

4.5.2 Organ motion

An important issue for the conventional 3D and the inverse treatment planning is the motion of organs. Not only the organs at risk but also the target volume can change position during the treatment course. There are different techniques to make sure that the applied dose is actually delivered to the correct place [41]. One possible way is to create a safety margin around the target. This technique is well established in conventional treatment [74]. For IMRT this additional margin would reduce the possible benefits of steep dose gradients between the target and neighboring OARs. For heavy, charged particle treatment planning, one must also take into account that a Bragg peak positioned right next to an OAR could deliver the peak dose right into the organ at risk if the organ moves towards the distal edge of the tumor.

Since organ motion is more pronounced in the lower parts of the body than in the head, a prostate patient was chosen for this study. Three IMRT plans were calculated. A photon IMRT plan which serves as the reference standard and two proton IMRT plans, one with the distal edge tracking technique and one with the 3D technique. All plans have the same number of beams (five) and are calculated on the same resolution dose grid and with the same organ parameters (see table 4.2). To simulate the movement of the target during the application of the optimized fluence profiles, two additional target volumes TP and TM were created. To define the new contours, the target volume was shifted by ±3 mm in the anterior and posterior (AP) direction (see figure 4.9).

To analyze the effect of organ motion, the minimum and maximum dose to the shifted target volumes (TP and TM) were compared with those for the original target volume (see table 4.7). The optimized plans are normalized to the median value of the original target volume.

The change in the maximum dose level and for the median dose of the target is negligible for all three modalities. This is due to the boost volume inside the

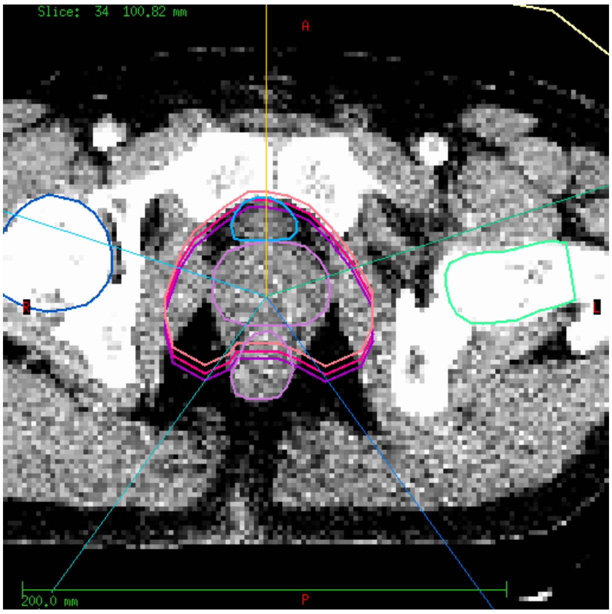

Figure 4.9: *Prostate patient: The target volume (dark red) was shifted by* ±3 *mm in the AP direction to create two new target volumes. TP (cyan) and TM (orange).*

target. The maximum dose is either located inside or at the edge of the boost volume. A totally different situation occurs for the minimum dose value. For the IMXT plan the maximum change is less than 5% but for both proton delivery techniques the minimum dose is reduced from about 52 Gy to about 38 Gy if the median value of the target is set to 72 Gy.

The comparison of the dose-volume histogram of the shifted profiles with the reference standard DVH of the target is shown in figure 4.10. The DVH for the photon TM contour has the smallest deviation compared to the original target DVH. The DVH for the DET and 3D technique are the same within ±4% for both shifted target volumes.

The larger deviation in the DVH and the minimum dose value for the heavy, charged particles is due to the steeper dose gradient at the edge of the target volume. For photons, the gradient is not as steep so that a movement of the target volume has a very small effect on the treatment plan.

Thus for heavy, charged particle IMRT a steeper gradient can be achieved than for photon IMRT. The disadvantage of the resulting dose distribution is that the treatment plan is more sensitive to organ motion. No significant difference between the DET and 3D technique was observed.

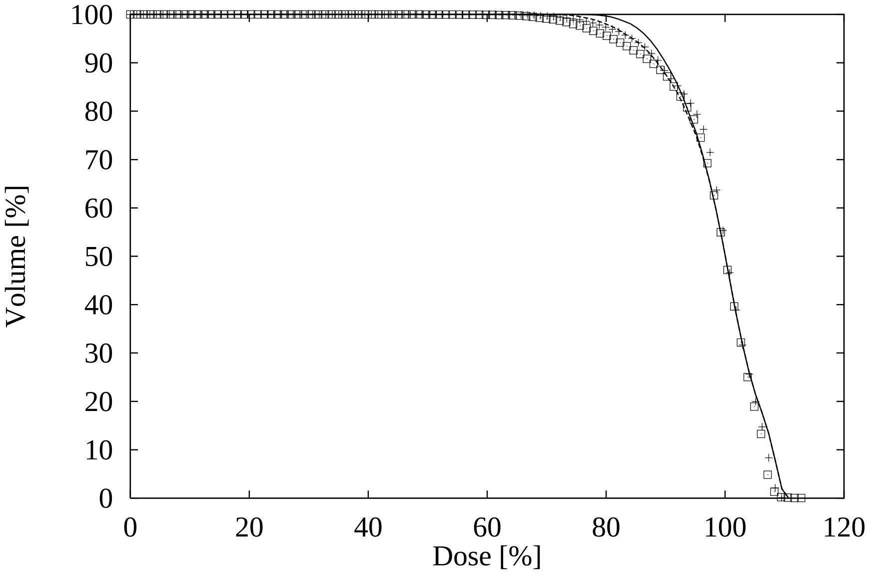

Figure 4.10: *Prostate: Comparison of the DVH for the TM contour (dashed line: photon, cross: DET, square box: 3D). The solid line is the DVH of the original photon plan.*

4.5.3 Range uncertainties

The comparison of the possibilities for the DET and 3D technique has shown no significant difference in the optimized dose distributions. The effect of organ motion has also been shown to be the same for both techniques. The last test to evaluate and compare the two delivery techniques is to look at the effects of the errors in the positioning of the spots.

To simulate a systematic error in the delivery device, the range shifter value for every spot was changed by $-3\,\mathrm{mm}$. By decreasing the range shifter (RS) the Bragg peak is shifted outside the tumor. This is a dangerous situation, especially in the case of a prostate patient where the rectum and bladder are located directly next to the target. Another problem is the error introduced during the conversion from Hounsfield units (HU) to relative stopping power. Any error in the relative stopping power changes the position of the Bragg peak. To simulate this error, the two plans were recalculated with a 5% reduction of the Hounsfield units [48]. This also results in an increased range of the particle beam.

Table 4.8 contains the results of the original IMPT plan and the recalculated treatment plans. The original plan is normalized to the median dose in the target. The values for the recalculated plan are normalized to the median dose of the original plan.

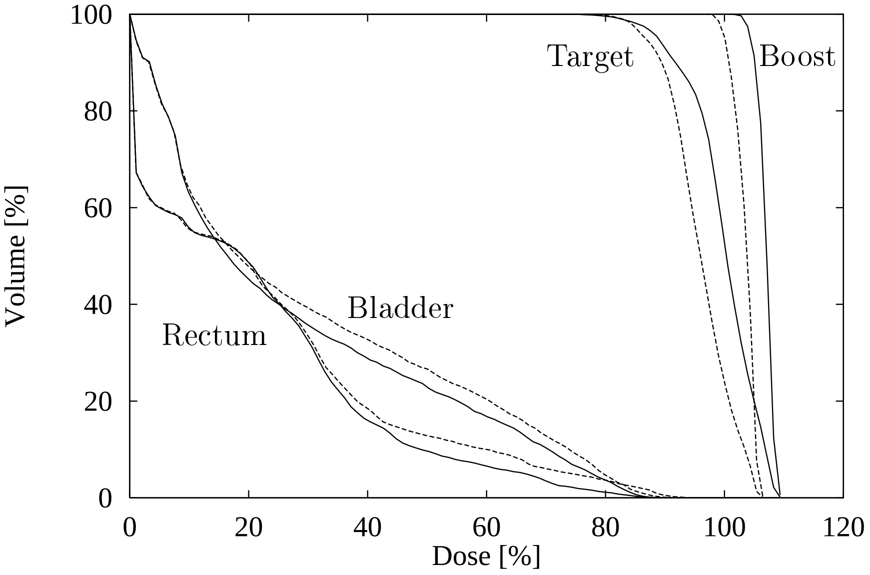

(a) *DET*

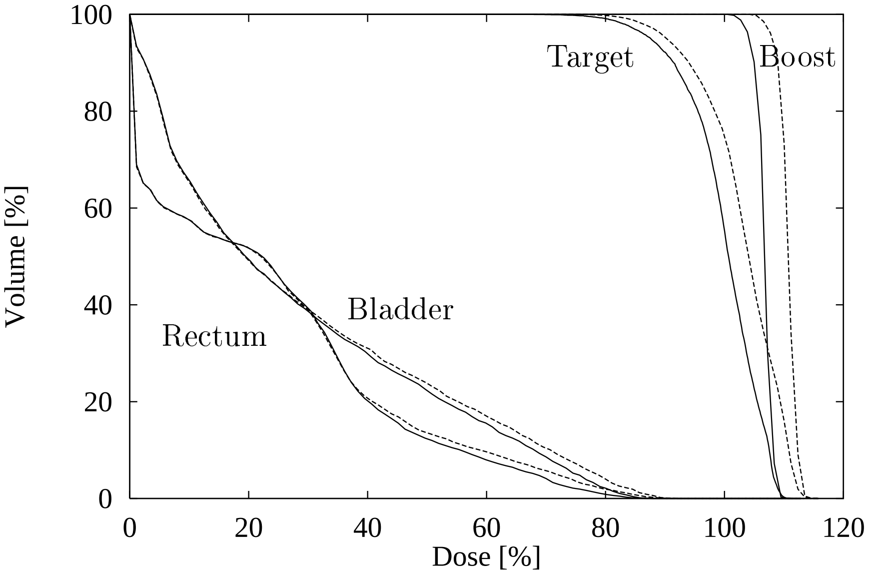

(b) *3D*

Figure 4.11: *Prostate: Comparison of two IMPT plans. The solid line is the original IMPT treatment plan. The dashed line is the result of a range shifter reduction of* $-3\,mm$*. (a) DET technique (b) 3D technique.*

	DET			3D		
	Org.	RS $-3\,\text{mm}$	HU -5%	Org.	RS $-3\,\text{mm}$	HU -5%
Min. target [%]	72.2	76.6	67.0	71.3	71.8	72.9
Max. target [%]	109.4	106.4	111.6	113.2	115.8	113.9
Median target [%]	100.0	96.0	101.3	100.0	103.7	99.1
Min. boost [%]	101.7	97.9	102.7	101.6	105.4	100.2
Max. boost [%]	109.4	106.4	110.5	109.5	113.5	108.2
Median boost [%]	107.4	103.7	108.1	106.8	110.7	105.6
Max. rectum [%]	91.9	93.6	87.1	85.9	89.2	85.4
Max. bladder [%]	90.8	92.6	89.3	87.1	91.5	85.4

Table 4.8: *Prostate: Comparison of the original IMPT plan, the recalculated treatment plan with a range shifter (RS) reduction of* 3 *mm and the result based on the a* 5% *reduced CT cube (HU).*

The DVH shown in figure 4.11(a) is the comparison of original IMPT DET plan and the plan with the reduced range shifter. The median values for the target and the boost volume are reduced by approximately 4%. As expected, the integral dose delivered to the rectum and the bladder is increased. For the 3D technique the DVH graph shows a is different effect of the range shifter than for the DET plan (see figure 4.11(b)): The median dose of the target and the boost volume is increased by 4%. Again the integral dose for the rectum and the bladder is increased.

Changing the range shifter values has different effects for the the DET and the 3D plan. For the distal edge tracking technique, the beam spots, which are only located at the edge of the target volume, are pushed outside the target volume. This leads to an increased minimum target dose level since the spots now cover a larger area but the same effect leads to a reduction of the dose homogeneity and a lower maximum dose level and therefore to a lower median value. For the 3D technique, beam spots are not only placed at the edge of the target volume but also inside the target and the boost volume. The dose distribution from one beam direction has the peak at the proximal edge of the target volume. Therefore, if the range shifter value is decreased, the peak positions are shifted towards the center of the target volume. The superposition of all beams leads to a higher maximum value. In figure 4.12 the depth-dose curves for a water phantom calculation of two 3D proton beams with a gantry angle of 0 and 180 degree (solid lines) and with a 3 mm range shifter reduction (dashed line) are given. The reduction of the

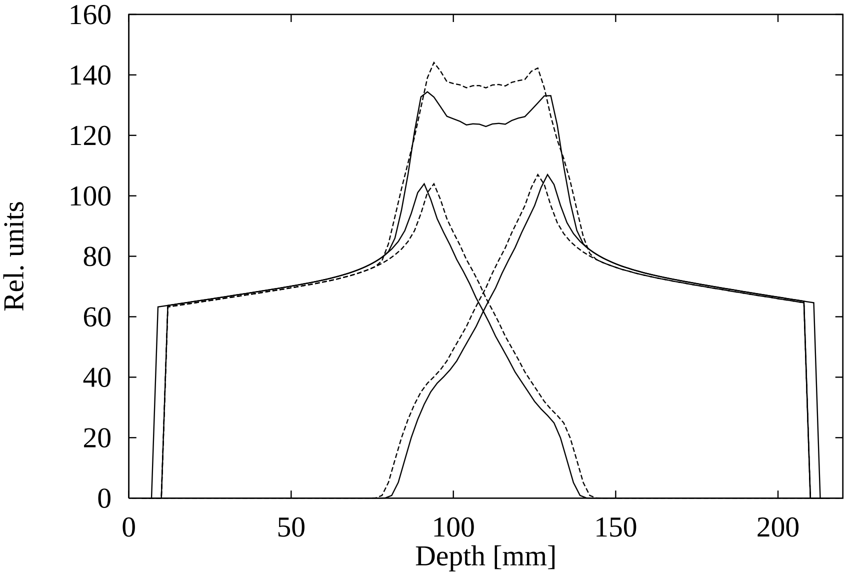

Figure 4.12: *Water phantom: Depth-dose distributions for two 3D beams with a gantry angle of 0 and 180 degree. The optimized depth-dose distributions for both beams (solid lines) are given. A reduction of the range shifter value by* 3 *mm leads to peak positions which are shifted towards the middle of the target volume (d=110) and to a higher maximum value in superposition of both depth-dose distributions.*

range shifter value results in peak positions which are shifted towards the middle of the target volume (depth = 110 mm). Also the superposition of the shifted dose distributions leads to a increased maximum value.

For both plans the median values of the target and the boost volume are changed by 4%. The underdosage and the overdosage of the target volumes for both delivery techniques is undesirable.

The results of the plan recalculated with a 5% shift in Hounsfield values differ from the range shifter results. For the plan with the changed range shifter values all beam spots are shifted by the same value. For the plan with the changed Hounsfield values, each beam spot is shifted by a different value. This leads to a significant reduction of the minimum target dose for the DET technique but not for the 3D technique. The regular grid for the 3D technique with a distance of 3 mm for the beam spots in beam direction is now replaced with a non-equidistant grid. This leads to a reduction of the median dose for the 3D technique. For both techniques the median and the maximum values for the target and the boost volume differ from the original plans by less than 2%.

	Photon	Proton	Proton + Photon
Nr. of beams	7	7-DET	1-3D + 7
Objective value	4120	4255	3714
Target: Minimum dose [%]	42.1	47.2	44.35
Target: Maximum dose [%]	123.9	124.3	118.6
Brainstem: Maximum dose [%]	76.6	74.5	70.7
Total dose: [a. u.]	1.0	0.49	0.90

Table 4.9: *Clivus chordoma: Comparison of different treatment modalities. A* $\sigma_{x,y} = 9\,mm$ *is used for the proton IMRT plans. All plans are normalized to the corresponding median target dose.*

The conclusion of the three comparisons is that by using the DET technique, an optimized dose distribution can be achieved which is at least as good as the 3D treatment plan. When compared to the photon IMRT plan, the DET plan gives a superior dose distribution, but is more sensitive to organ motion.

4.6 Simultaneous optimization of a plan with photon and proton beams

The possibility of simultaneous optimization of different radiation modalities is another advantage of the new planning tool. The optimization is done with a single set of organ parameters. The same resolution for the dose grid for all plans was used.

A plan with the combination of protons and photon was created. One might wonder why a combination of photons and protons would be used, if proton IMRT is also available. Up to now all treatment plans were created with a $\sigma_{x,y}$ of 2.5 mm. Such a small sigma value is only available at few facilities. Other sites can for example have a larger $\sigma_{x,y}$ of about 9 mm. With that beam, the optimized IMPT plans are not as good as for the other treatment device. In this case a combination of proton and photon IMRT could be used.

The reference standard for this comparison is again the seven-beam photon IMRT plan. For the proton plans a lateral scanning grid of 9 mm was used. For the 3D technique the distance between two spots in beam direction was set to 3 mm.

From the values in table 4.9, the DET technique seems equivalent to the photon IMRT plan. The DVH in figure 4.13 shows that the slope for the target is worse

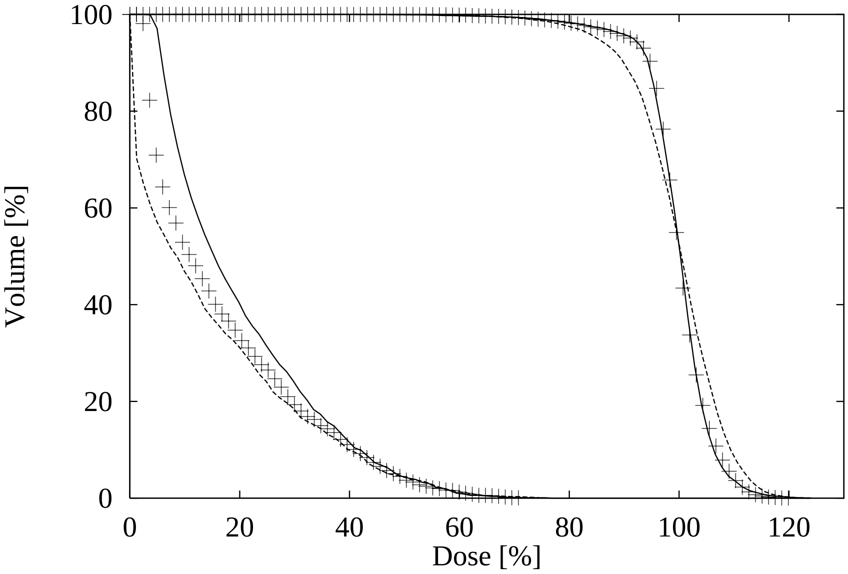

Figure 4.13: *Clivus chordoma: Dose-volume histogram of the photon IMRT plan (solid line), the proton DET plan (dashed line) and the combination of photon and protons (crosses).*

than for the IMXT plan. The combination of a proton 3D beam from $\phi_{\text{Gantry}} = 0^\circ$ and seven equidistant spaced photon beams leads to a target DVH similar to the IMXT plan. The DVH for the brainstem is not as good as for the DET IMPT plan but better than for the photon IMRT plan. Another benefit is the reduction of the total dose delivered to the patient by 10%. The mean integral dose for example is an important factor in the treatment of children [58].

Figure 4.14 shows the dose distribution for the transverse isocenter slice.

The combination of photon and proton modalities is only one option. Another example is the treatment of superficial tumors, where a combination of photons and electrons might be useful [38].

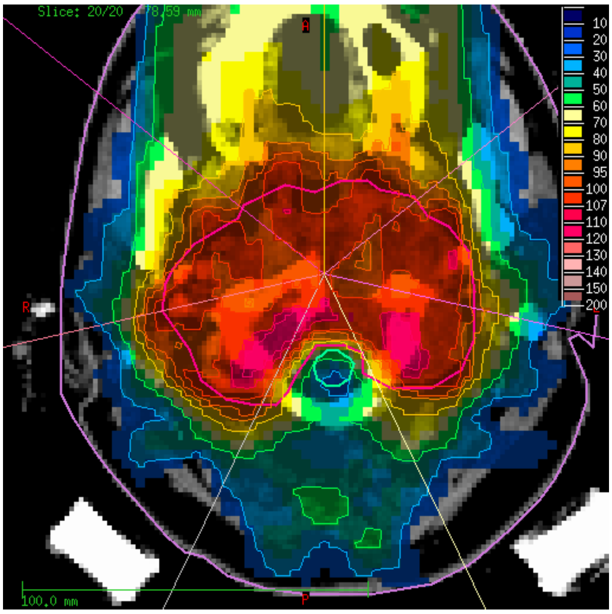

Figure 4.14: *Clivus chordoma: Dose distribution for the mixed IMRT plan. The dose distribution is normalized to the median target dose.*

Chapter 5

Discussion & Conclusion

Design of a modular planning system

The modular design of the inverse treatment planning tool that has been developed, with separate optimization loop, dose calculation engine and graphical user interface, enables the simple expansion of the system or inclusion of new features. The implications of this design are discussed in the section.

D_{ij} matrix approach

The central component of the new, modular treatment planning system is the D_{ij} matrix. Due to the large amount of computer memory required for the storage of the D_{ij} matrix, the effect on the computing time of the system was analyzed. The optimization speed of the D_{ij} matrix approach was compared with the DKFZ routine system for photon IMRT plans [56]. The new system is slower by a factor of two compared with the integrate loop system, which uses a simple dose calculation model. There are two possible methods to improve the computational speed of the new planning tool without reducing the accuracy of the dose calculation. A first solution is, as explained in section 2.3, that only voxels within a certain distance from the central ray of the selected bixels are stored in the D_{ij} matrix [20]. The speed of the optimization loop increases linearly with reduction of the number of elements in the D_{ij} matrix. The second possible way is to mask all voxels except for those within the target or organs at risk, therefore the dose to the normal tissue is not calculated during the optimization.

Optimization loop

The modular design of the new planning system makes it possible to use different optimization algorithms and objective functions inside the optimization loop. Bortfeld et al. [6] used a Newton gradient approach to find the optimal solution. The experience with this algorithm has shown that it is a fast and reliable optimization method. Therefore, the Newton gradient approach was modified to make use of the D_{ij} matrix and the damping factor was adapted to the new concept. Lomax et al. [47] also applied the Newton gradient method [27] but with a different damping factor. Other methods like simulated annealing [73] or a conjugate gradient method [70] can also be integrated into the system.

The use of the D_{ij} matrix concept allows lateral scattering to be accounted for within the optimization loop during the updating of the bixel weights. This is true not only for photons, but for all radiation modalities. In the treatment planning tool developed by Preiser et al. [56], lateral scatter was only taken into account during the calculation of the 3D dose distribution based on the current fluence distribution. During the update of the fluence matrices the dose distributions simply along the central ray of the bixel were used. This limitation is removed with the D_{ij} matrix approach and leads to a better sparing of organs at risk next to the target volume. This effect was shown in section 4.3 for the clivus chordoma patient.

Another important benefit of the new planning tool is the potential application of improved dose calculation algorithms compared to the simplified algorithms used in most existing planning tools. Therefore time consuming algorithms like Monte Carlo or superposition can be used during the optimization process. This is feasible because the dose calculation to create the D_{ij} matrix needs only to be done once before the optimization loop starts. With other IMRT tools which are using the integrated loop, a full dose calculation must be done for every iteration step and therefore the use of more sophisticated and time consuming dose calculations algorithms like Monte Carlo are not possible. Some treatment planning tools have therefore developed a hybrid model [42, 68]. First a simple pencil beam dose calculation is employed during the optimization. The resulting fluence distributions are used as the starting solutions for the Monte Carlo or superposition optimization. By using the output of the first optimization process, only a few iteration steps must be performed with the more time consuming algorithms.

Dose delivery modes

For the optimization and the delivery of heavy, charged particles to the patient, two different techniques were presented, first the distal edge tracking technique proposed by Deasy et al. [21] and second the 3D technique [16, 17]. To find the correct beam spot positions at the edge of the target volume, an algorithm was developed in section 2.5.2.1. The comparison of the calculated and the prescribed beam spot positions showed that all spots were within 1 mm of the desired positions. Other available delivery techniques like the 2D or 2.5D technique [47] can also be optimized with the new planning tool but in this thesis only the most demanding and advanced delivery techniques were studied.

Accurate dose calculation

To calculate the D_{ij} matrix two dose algorithms were developed. First a finite pencil beam algorithm for photon IMRT was developed. Most other photons IMRT tools use similar photon pencil beam algorithms [25]. To test the dose calculation module, measured data were compared with calculated results. The agreement was within 2%. The finite pencil beam uses a radiological depth scaling to take inhomogeneities into account. As a first order approximation, electron treatments can also be treated this way. The use of other dose calculations like Monte Carlo for photon IMRT is not yet studied to the full extent. For example Laub et al. [43] report no significant differences for the target DVH in one case but an improvement for an other case [42]. Further studies are necessary to come to a conclusion.

A second algorithm especially for heavy, charged particles was developed, again based on the pencil beam technique. The input data for the central part of the pencil beam algorithm are measured depth-dose data. By using measured data, energy straggling and also for example the fragmentation of carbon is taken into account. The lateral part of the pencil beam is modeled by two Gaussian distributions, one for the initial phase space of the incident beam and one for the multiple Coulomb scattering inside the patient. The broadening of the beam is taken into account by a depth dependent sigma value. This is a standard procedure for modeling a particle beam [23, 28, 60]. The inhomogeneities were account for through the same radiological depth scaling algorithm as for photons. Schaffner et al. [62] have shown the difference between the pencil beam calculation and the Monte Carlo calculation [72] for a water phantom with a inhomogeneity slab placed perpendicular to the beam direction. For the selected setup the differences could not be neglected. However, for most tumor locations radiological depth scaling is expected to be sufficient.

Application of a multi-modality inverse treatment planning system

To show the potential of the new planning tool, two typical IMRT patients were selected for the application of the new planning tool. The first patient suffers from a clivus chordoma tumor. Because of the concave shape of the tumor and the location next to the brainstem, this patient is a typical photon IMRT patient. For the second case a prostate tumor was selected and therefore the bladder and the rectum are the most crucial organs at risk.

To demonstrate the new possibility to optimize different radiation modalities within the same treatment system, IMRT plans for photons, electrons, protons (DET) and carbon ions for both patients are created. The geometrical setup, the voxel resolution and the organ parameters were chosen to be the same for all modalities. Because the organ parameters were set to achieve the best possible photon IMRT plan, the resulting proton and carbon ion dose distributions can as expected also fulfill the specified objectives. The electron IMRT plan has the worst (highest) objective value. This is due to the deep location of the target volume and the physical depth-dose characteristics of the electron beam. But it is important to keep in mind, that if a plan has a slightly lower objective function value, it is not always better in a clinical sense. For an exhaustive comparison, the minimum and maximum value of the different organs, the DVH and even the 3D dose distribution must also be taken into account.

Comparison of photon and proton IMRT plans

Bortfeld [7] has shown the possibilities and the limits of the use of external beam radiation. The conclusion of his work was that by using IMXT almost every dose conformation required could be achieved. Only for special cases did the use of heavy, charged particles lead to significantly better results. Lomax et al. [49] compared IMXT to conventional proton therapy. It was shown that by using IMXT the same target coverage as for the conventional protons plan could be achieved. However, it was also reported that for a better comparison the inverse planning method for both radiation modalities must be applied. Therefore in section 4.4.1 a seven beam photon IMRT plan is compared with a seven beam proton DET IMRT plan for the clivus chordoma patient. It was shown that the IMPT plan covers the target volume for this case even better than the IMXT plan. With IMPT also the maximum and integral dose delivered to the brainstem is reduced significantly. These findings are in good agreement with comparisons for other tumor locations. Mirabelle et al. [52] compared both modalities for orbital and paraorbital tumors and Cella et al. [19] compared the modalities for prostate cancer.

Potential of the DET and 3D technique for protons

For heavy, charged particles there are four possible application methods [47]. The two most promising methods, the DET and the 3D technique were analyzed and compared with the photon IMRT plan. Lomax et al. [47] have shown that for a large number of incident beams the DET and the 3D technique result in very similar dose distributions. The comparisons of the DET and 3D technique for a different number of beam directions in section 4.5.1 have shown that the beam directions could be reduced from seven to five without significantly reducing the quality of the DET dose distributions. The target coverage of the five beams DET IMPT plan is even better than for the seven beam photon IMRT plan. Therefore in contrast to the results of Lomax et al. [47], a good target coverage could be achieved with the DET technique even with a reduced number of beams. The reduction of the number of beams for the 3D technique also leads to a reduction of the plan quality but not as fast as for the DET technique. Another important advantage of the DET technique is the smaller number of required beam spots compared to the 3D technique. For the clivus chordoma patient the number of beam spots for the DET technique compared to the 3D technique and therefore the optimization time and also the expected delivery time is reduced by a factor of ten.

After the comparison of the DET and the 3D technique for a static target the influence of organ motion on both optimized treatment plans was studied for the prostate patient. The defined target volume was shifted by $\pm 3\,\mathrm{mm}$ along the anterior-posterior direction. The results showed that there is no significant difference for a five beam plan between the 3D and the DET technique. For both delivery techniques the minimum target dose is reduced more than for the photon IMRT plan. This is due to the steeper dose gradient of the particle IMRT plans. Because of this effect, it is more important for particle therapy to develop methods to include organ motion during treatment planning, as done by Li et al. [45] and Löf et al. [46]. So far, the methods are compromised because no reliable model for the organ motion itself is available. An alternative method is to take a CT image of the patient immediately before treatment and adapt the fluence profile to the new positions of the target and the organs at risk on a daily basis [78].

Because of the physical depth-dose characteristic the uncertainty in the range of the particle beam is another important issue for heavy, charged particle therapy.

The mispositioning of the Bragg peak can be either the result of a systematic error in the delivery device or an inaccuracy in the conversion of the Hounsfield units to relative stopping power. To simulate these problems, the optimized IMPT plans for the prostate patient were recalculated first with range shifter values reduced by 3 mm and second with a modified CT cube where the Hounsfield values have been changed by -5%. The differences between the original optimized plan and the recalculated one with the modified CT cube is, for both proton delivery techniques, below 1.5% for the median target value. This is not true for the modified range shifter values. In this case the median target dose for the DET technique is reduced, whereas for the 3D technique the median target dose is increased. Due to the reduction of the range shifter values and the reduced CT Hounsfield units the Bragg peak positions are shifted outside the target volume. To protect organs at risk next to the target volume, Lomax et al. [48] selected beam directions which avoid the positioning of Bragg peaks directly in front of organs at risk.

The comparison between the DET and the 3D technique showed that no significant difference exists in the dose distributions or for the sensitivity to organ motion. Also the differences observed between the dose distributions of the original and the recalculated plans with modified peak positions for both delivery techniques are the same order of magnitude. Therefore considering the lower number of spots and the reduced computing and treatment time for DET, the DET is a good alternative to the conventional favorite 3D technique. One problem of the DET technique could be the biological effect of the particle beam. For the proton Bragg peak, a higher RBE value is measured only at the distal edge of the dose distribution [54]. Therefore for the DET technique only the outside margin of the tumor is irradiated with a higher RBE value. Since for the 3D technique beam spots are placed all over the tumor volume, every part of the tumor is exposed at least once with a higher RBE value. Further studies are necessary to analyze this effect.

Optimization of combined modality irradiations

The results presented in chapter 4 show that the newly developed multi-modality IMRT treatment planning tool is capable of creating optimized dose distributions for different radiation modalities and delivery techniques. Most other treatment planning system are only designed for the use of a single radiation modality. E.g., the system used at the DKFZ for the routine treatment planning, which was developed by Preiser et al. [56], is only able to optimize photons like many other TP systems [1, 18, 70]. Specialized to heavy, charged particles, such as the systems by Lomax et al. [47] and Krämer et al. [39], are only able to optimize protons or carbon ions. Only the system by Korevaar et al. [38] can optimize electron and photon IMRT plans at the same time. As shown in section 4.6, the simultaneous optimization of photon and proton IMRT beams could lead to an interesting dose distribution which is superior to the photon IMRT plan.

Another interesting field for simultaneous optimization of photons and electrons is the treatment of superficial tumors like breast carcinoma. Photon breast IMRT leads only to minor improvements in the dose distributions compared to 3D non-IMRT techniques [2, 37]. Further studies have to show whether the simultaneous optimization of the electron and the photon fields can lead to better dose distributions.

Chapter 6

Summary & Outlook

The new treatment planning system described by this thesis opens new possibilities for the inverse treatment planning process. The modular design for the optimization loop, the dose engine and the graphical user interface allows for expansion of all parts of the system in a simple and efficient way, e.g. the integration of new optimization algorithms, objective functions or future dose calculation algorithms into the new planning tool. The introduction of the D_{ij} matrix concept enables the use of improved dose calculation algorithms during the optimization process. Therefore the application of time consuming algorithms like Monte Carlo or superposition becomes available. Another benefit of the D_{ij} matrix approach is the possibility to optimize radiation therapy for most radiation modalities within one single system. Furthermore, one can perform simultaneous optimization of different radiation modalities for one patient.

The application of this newly developed planning tool to two patients using the radiation modalities of photons, protons, carbon ions and electrons demonstrates the potential of the new planning tool. The comparison of photon and proton IMRT plans confirmed the expected potential of heavy, charged particle IMRT. The study of the different delivery techniques for heavy, charged particle IMRT has shown that the use of the distal edge tracking techniques offers a good alternative to the established 3D technique even for a small number of beams directions. The result of the simultaneous optimization of a photon and proton IMRT plan enables an outlook on the capabilities of simultaneous optimization of two or more different radiation modalities.

The extension of the optimization loop with biologically motivated objective functions for different radiation modalities and the integration of RBE models for heavy, charged particles are projects for the near future. Moreover the automatic selection of beam directions should be integrated into the planning tool. For heavy, charged particles the beam selection algorithm should take the higher

RBE value at the distal edge of the depth-dose distribution of the Bragg peak into account. This could reduce the risk of a possible irradiation of organs at risk due to organ motion. The potential of the simultaneous optimization of different radiation modalities has not been exhaustively studied yet. However the new available planning tool has the potential for further exciting investigations. By using the newly available planning tool the potential can now be explored. Especially the combination of photon and electrons for superficial tumors is of great interest. With the construction of modern heavy, charged particle facilities in different countries in the near future, a modern planning tool is required. The multi-modality inverse treatment planning tool that has been developed can help to satisfy this demand.

List of Figures

List of Tables

Bibliography

[1] M. Alber. *A Concept for the Optimization of Radiotherapy.* PhD thesis, Universität Tübingen, 2000.

[2] A. Aref, D. Thornton, E. Youssef, T. He, S. Tekyi-Mensah, L. Denton, and G. Ezzell. Dosimetric improvements following 3D planning of tangential breast irradiation. *Int. J. Radiation Oncology Biol. Phys.*, 48(5):1569–1574, 2000.

[3] R. M. Barnett et al. Particles and fields. *Physical Review D*, 54(1), 1996. and 1997 off-year partial update for the 1998 edition.

[4] R. Bendl, J. Pross, A. Höss, MA. Keller, K. Preiser, and W. Schlegel. VIRTUOS - a program for virtual radiotherapy simulation and verification. In *Proceeding of XI Int. Conf. on the Use of Computers in Radiation Therapy, Manchester, UK*, pages 226–227, 1994.

[5] S. Boon. *Dosimetry and quality control of scanning proton beams.* PhD thesis, University of Groningen, 1998. ISBN 90-367-0952-0.

[6] T. Bortfeld. *Neue Methoden zur Lösung des inversen Problems der Strahlentherapieplanung.* PhD thesis, Ruprechts-Karls-Universität Heidelberg, 1990.

[7] T. Bortfeld. Dosiskonformation in der Tumortherapie mit externer ionisierender Strahlung: Physikalische Möglichkeiten und Grenzen. Habilitationsschrift, Ruprechts-Karls-Universität Heidelberg, 1995.

[8] T. Bortfeld. An analytical approximation of the Bragg curve for therapeutic proton beams. *Medical Physics*, 24(12):2024–2033, 1997.

[9] T. Bortfeld, J. Bürkelbach, R. Boesecke, and W. Schlegel. Methods of image reconstruction from projections applied to conformation radiotherapy. *Physics in Medicine and Biology*, 35:1423–1434, 1990.

[10] T. Bortfeld, U. Oelfke, and S. Nill. What is the optimum leaf width of a multileaf collimator. *Medical Physics*, 27(11):2494–2501, 2000.

[11] T. Bortfeld and W. Schlegel. An analytical approximation of depth-dose distributions for therapeutic proton beams. *Physics in Medicine and Biology*, 41:1331–1339, 1996.

[12] T. Bortfeld, W. Schlegel, and B. Rhein. Decomposition of pencil beam kernels for fast dose calculations in three-dimensional treatment planning. *Medical Physics*, 20(2):311–318, 1993.

[13] T. Bortfeld, J. Stein, and K. Preiser. Clinically relevant intensity modulation optimization using physical constraints. In *Proceeding of XII Int. Conf. on the Use of Computers in Radiation Therapy, Salt Lake City, Utah*, pages 1–4, 1997.

[14] A. Brahme. Optimization of stationary and moving beam radiation therapy techniques. *Radiotherapy and Oncology*, 12(2):129–140, 1988.

[15] A. Brahme. Individualizing cancer treatment: biological optimization models in treatment planning and delivery. *Int. J. Radiation Oncology Biol. Phys.*, 49(2):327–337, 2001.

[16] A. Brahme, P. Källman, and B. K. Lind. Optimization of proton and heavy ion therapy using an adaptive inversion algorithm. *Radiotherapy and Oncology*, 15:189–197, 1989.

[17] Å. K. Carlsson, P. Andreo, and A. Brahme. Monte Carlo and analytical calculation of proton pencil beams for computerized treatment plan optimization. *Physics in Medicine and Biology*, 42:1033–1053, 1997.

[18] M. Carol. Integrated 3D conformal multivane intensity modulation delivery system for radiotherapy. In *Proceeding of XI Int. Conf. on the Use of Computers in Radiation Therapy, Manchester, UK*, pages 172–173, 1994.

[19] L. Cella, A. J. Lomax, and R. Miralbell. Potential role of intensity modulated proton beams in prostate cancer radiotherapy. *Int. J. Radiation Oncology Biol. Phys.*, 49(1):217–223, 2001.

[20] P. S. Cho and M. H. Phillips. Reduction of computational dimensionality in inverse radiotherapy planning use sparse matrix operations. *Physics in Medicine and Biology*, 46:N117–N125, 2001.

[21] J. O. Deasy, D. M. Shephard, and T. R. Mackie. Distal edge tracking: a proposed delivery method for conformal proton therapy using intensity modulation. In *Proceeding of XII Int. Conf. on the Use of Computers in Radiation Therapy, Salt Lake City, Utah*, pages 406–409, 1997.

[22] S. S. Donaldson, A. L. Boyer, and W. R. Hendee. New methods for precision radiation therapy exceed biological and clinical knowledge and institutional resources needed for implementation. *Medical Physics*, 27(11):2477–2479, 2000.

[23] K.U. Gardey. *A Pencil Beam Model for Proton Therapy - Treatment Planning and Experimental Results.* PhD thesis, Ruprechts-Karls-Universität Heidelberg, 1996.

[24] B. Gottschalk, A. M. Koehler, R. J. Scheider, J. M. Sisterson, and M. S. Wagner. Multiple coulomb scattering of 160 MeV protons. *Nucl. Instrum. Method*, B74:467–490, 1993.

[25] A. Gustafsson, B. K. Lind, and A. Brahme. A generalized pencil beam algorithm for optimization of radiation therapy. *Medical Physics*, 21(3):343–356, 1994.

[26] Th. Haberer, W. Becher, D. Schardt, and G. Kraft. Magnetic scanning system for heavy ion therapy. *Nucl. Instr. and Meth. in Phys. Res. A*, 330:296–305, 1993.

[27] T. Holmes and T. R. Mackie. A comparison of three inverse treatment planning algorithms. *Physics in Medicine and Biology*, 39:91–106, 1994.

[28] L. Hong, M. Goitein, M. Bucciolini, R. Comiskey, B. Gottschalk, S. Rosenthal, C. Serago, and M. Urie. A pencil beam algorithm for proton dose calculations. *Physics in Medicine and Biology*, 41:1305–1330, 1996.

[29] G. Hounsfield. A method of and apparatus for examination of a body by radiation such as x or g radiation. British patent nro. 1283915, London. Issued to EMI Ltd Application filed Aug. 1968.

[30] ICRU Report 50: Prescribing, recording, and reporting photon beam therapy. International Commission on Radiation Units and Measurements, Bethesda, Maryland, USA, 1993.

[31] IEC. *IEC 61217 (1996-08): Radiotherapy equipment - Coordinates, movements and scales.* International Electrotechnical Commission, 1996.

[32] IEC. *IEC 61217-am1 (2000-12): Amendment 1.* International Electrotechnical Commission, 2000.

[33] J. D. Jackson. *Classical Electrodynamics.* John Wiley & Sons, third edition, 1998.

[34] O. Jäkel, C. Jacob, D. Schardt, CP. Karger, and GH. Hartmann. Relation between carbon ion ranges and x-ray CT numbers. *Medical Physics*, 28(4):701–703, 2001.

[35] PJ. Keall and PW. Hoban. A review of electron beam dose calculation algorithms. *Australas Phys Eng Sci Med*, 19(3):111–130, 1996.

[36] A. Kessen. Integration eines neuen Dosisberechnungsverfahrens in die inverse Strahlentherapieplanung mit Photonen. Diplomarbeit, Ruprechts-Karls-Universität Heidelberg, 2000.

[37] L. L. Kestin, M. B. Sharpe, R. C. Frazier, F. A. Vicini, D. Yan, R. C. Matter, A. A. Martinez, and J. W. Wong. Intensity modulation to improve dose uniformity with tangential breast radiotherapy: Initial clinical experience. *Int. J. Radiation Oncology Biol. Phys.*, 48(5):1559–1568, 2000.

[38] E. W Korevaar, B. J M Heijmen, E. Woudstra, H. Huizenga, and A. Brahme. Mixing intensity modulated electron and photon beams: combining a steep dose fall-of at depth with sharp and depth-independent penumbras and flat beam profiles. *Physics in Medicine and Biology*, 44:2171–2181, 1999.

[39] M. Krämer, O. Jäkel, T. Haberer, G. Kraft, D. Schardt, and U. Weber. Treatment planning for heavy-ion radiotherapy: physical beam model and dose optimization. *Physics in Medicine and Biology*, 45(11):3299–3317, 2000.

[40] M. Krämer and M. Scholz. Treatment planning for heavy-ion radiotherapy: calculation and optimization of biologically effective dose. *Physics in Medicine and Biology*, 45(11):3319–3330, 2000.

[41] KM. Langen and DT. Jones. Organ motion and its management. *Int. J. Radiation Oncology Biol. Phys.*, 50(1):265–278, 2001.

[42] W. Laub, M. Alber, M. Birkner, and F. Nüsslin. Monte Carlo dose computation for IMRT optimization. *Physics in Medicine and Biology*, 45(7):1741–1754, 2000.

[43] W. Laub, A. Bakai, and F. Nüsslin. Intensity modulated irradiation of a thorax phantom: comparisons between measurements, Monte Carlo calculations and pencil beam calculations. *Physics in Medicine and Biology*, 46(6):1695–1706, 2001.

[44] S. Levegrün, A. Jackson, MJ. Zelefsky, ES. Venkatraman, MW. Skwarchuk, W. Schlegel, Z. Fuks, SA. Leibel, and CC. Ling. Analysis of biopsy outcome after 3D conformal radiation therapy of prostate cancer using dose-

distribution variables and tumor control probability models. *Int. J. Radiation Oncology Biol. Phys.*, 47:1245–1260, 2000.

[45] J. G. Li and L. Xing. Inverse planning incorporating organ motion. *Medical Physics*, 28(7):1573–1578, 2000.

[46] J. Löf, B. K Lind, and A. Brahme. An adaptive control algorithm for optimization of intensity modulated radiotherapy considering uncertainties in beam profiles, patient set-up and internal organ motion. *Physics in Medicine and Biology*, 43:1605–1628, 1998.

[47] A. J. Lomax. Intensity modulation methods for proton radiotherapy. *Physics in Medicine and Biology*, 44:185–205, 1999.

[48] A. J. Lomax, T. Boehringer, A. Coray, E. Egger, G. Goitein, M. Grossmann, P. Juelke, S. Lin, E. Pedroni, B. Rohrer, W. Roser, B. Rossi, B. Siegenthaler, O. Stadelmann, H. Stauble, C. Vetter, and L. Wisser. Intensity modulated proton therapy: A clinical example. *Medical Physics*, 28(3):317–324, 2001.

[49] A. J. Lomax, T. Bortfeld, G. Goitein, J. Debus, C. Dykstra, PA. Tercier, PA. Coucke, and RO. Mirimanoff. A treatment planning inter-comparison of proton and intensity modulated photon radiotherapy. *Radiotherapy and Oncology*, 51:257–271, 1999.

[50] S. Lorin, E. Grusell, N. Tilly, J. Medin, M. Blom, V. Ziemann, D. Reistad, and B. Glimelius. Development of a compact proton scanning system in uppsala with a moveable second magnet. *Physics in Medicine and Biology*, 45(5):1151–1163, 2000.

[51] M. Mehta, R. Scrimger, R. Mackie, B. Paliwal, R. Chappell, and J. Fowler. A new approach to dose escalation in non-small-cell lung cancer. *Int. J. Radiation Oncology Biol. Phys.*, 49:23–33, 2001.

[52] R. Miralbell, L. Cella, D. Weber, and A. J. Lomax. Optimizing radiotherapy of orbital and paraorbital tumors: intensity-modulated x-ray beams vs. intensity-modulated proton beams. *Int. J. Radiation Oncology Biol. Phys.*, 47(4):1111–1119, 2000.

[53] S. Nill, U. Oelfke, and T. Bortfeld. A new planning tool for IMRT treatment: Implementation and first application for proton beams. In *Proceeding of XIII Int. Conf. on the Use of Computers in Radiation Therapy, Heidelberg, Germany*, pages 326–328, 2000.

[54] H. Paganetti, P. Olko, H. Kobus, R. Becker, T. Schmitz, MP. Waligorski, D. Filges, and HW. Muller-Gartner. Calculation of relative biological effectiveness for proton beams using biological weighting functions. *Int. J. Radiation Oncology Biol. Phys.*, 37(3):719–729, 1997.

[55] E. Pedroni, R. Bacher, H. Blattmann, T. Bohringer, A. Coray, A. Lomax, S. Lin, G. Munkel, S. Scheib, U. Schneider, et al. The 200 MeV proton therapy project at the Paul Scherrer Institute: Conceptual design and practical realisation. *Medical Physics*, 22(1):37–53, 1995.

[56] K. Preiser, T. Bortfeld, K. Hartwig, W. Schlegel, and J. Stein. A new program for inverse radiotherapy planning. In *Proceeding of XII Int. Conf. on the Use of Computers in Radiation Therapy, Salt Lake City, Utah*, pages 425–428, 1997.

[57] LE. Reinstein, XH. Wang, CM. Burman, Z. Chen, R. Mohan, G. Kutcher, SA. Leibel, and Z. Fuks. A feasibility study of automated inverse treatment planning for cancer of the prostate. *Int. J. Radiation Oncology Biol. Phys.*, 40(1):207–214, 1998.

[58] E. Ron, B. Modan, JD. Boice, E. Alfandary, M. Stovall, A. Chetrit, and L. Katz. Tumors of the brain and nervous system after radiotherapy in childhood. *N Engl J Med*, 319:1033–1039, 1988.

[59] K. R. Russell, E. Grusell, and A. Montelius. Dose calculations in proton beams: range straggling corrections and energy scaling. *Physics in Medicine and Biology*, 40(6):1031–1043, 1995.

[60] K. R. Russell, U. Isacsson, M. Saxner, A. Ahnesjo, A. Montelius, E. Grusell, CV. Dahlgren, S. Lorin, and B. Glimelius. Implementation of pencil kernel and depth penetration algorithms for treatment planning of proton beams. *Physics in Medicine and Biology*, 45:9–27, 2000.

[61] B. Schaffner and E. Pedroni. The precision of proton range calculations in proton radiotherapy treatment planning: experimental verification of the relation between CT-HU and proton stopping power. *Physics in Medicine and Biology*, 43:1579–1592, 1998.

[62] B. Schaffner, E. Pedroni, and A. J. Lomax. Dose calculation models for proton treatment planning using a dynamic beam delivery system: an attempt to include density heterogeneity effects in the analytical dose calculation. *Physics in Medicine and Biology*, 44:27–41, 1999.

[63] S. G. Scheib. *Spot-Scanning mit Protonen: Experimentelle Resultate und Therapieplanung.* PhD thesis, Eidgenössische Technische Hochschule Zürich, 1994.

[64] S. G. Scheib and E. Pedroni. Dose calculation and optimization for 3D conformal voxel scanning. *Radiation and Environmental Biophysics*, 31:251–256, 1992.

[65] U. Schneider, E. Pedroni, and A. J. Lomax. The calibration of CT Hounsfield units for radiotherapy treatment planning. *Physics in Medicine and Biology*, 41(1):111–124, 1996.

[66] C. Schulze. *Entwicklung schneller Algorithmen zur Dosisberechnung für die Bestrahlung inhomogener Medien mit hochenergetischen Photonen.* PhD thesis, Ruprechts-Karls-Universität Heidelberg, 1995.

[67] R. L. Siddon. Calculation of the radiological depth. *Medical Physics*, 12(1):84–87, 1985.

[68] J. V. Siebers, S. Tong, M. Lauterbach, Q. Wu, and R. Mohan. Acceleration of dose calculations for intensity-modulated radiotherapy. *Medical Physics*, 28(6):903–910, 2001.

[69] J.M. Sisterson, editor. *Particles Newsletter 27*, 2001.

[70] S. V. Spirou and CS. Chui. Gradient inverse planning algorithm with dose-volume constraints. *Medical Physics*, 25(3):321–333, 1998.

[71] C. Thieke, S. Nill, U. Oelfke, and T. Bortfeld. Acceleration of IMRT dose calculation by importance-sampling of the calculation matrices. *Medical Physics*, 2001. submitted.

[72] A. Tourovsky, A. J. Lomax, E. Pedroni, and U. Scheider. Monte Carlo codes for proton radiography and treatment planning. PSI Life Sciences Newsletter, 1993.

[73] S. Webb. Optimisation of conformal radiotherapy dose distributions by simulated annealing. *Physics in Medicine and Biology*, 34(10):1349–1370, 1989.

[74] S. Webb. *The Physics of Conformal Radiotherapy: Advances in Technology.* Bristol: Institute of Physics Publishing, 1997.

[75] S. Webb. *Intensity-Modulated Radiation Therapy.* Bristol: Institute of Physics Publishing, 2001.

[76] Q. Wu and R. Mohan. Algorithms and functionality of an intensity modulated radiotherapy optimization system. *Medical Physics*, 27(4):701–711, 2000.

[77] L. Xing, J. G. Li, S. Donaldson, Q. T. Le, and A. L. Boyer. Optimization of importance factors in inverse planning. *Physics in Medicine and Biology*, 44:2525–2536, 1999.

[78] D. Yan, D. Lockman, D. Brabbins, L. Tyburski, and A. Martinez. An off-line strategy for constructing a patient-specific planning target volume in adaptive treatment process for prostate cancer. *Int. J. Radiation Oncology Biol. Phys.*, 48(1):289–302, 2000.

[79] K. Yoda, Y. Saito, and H. Sakamoto. Dose optimization of proton and heavy ion therapy using generalized sampled pattern matching. *Physics in Medicine and Biology*, 42:2411–2420, 1997.

Danksagung

Mein Dank gilt an erster Stelle Herrn Professor Dr. Thomas Bortfeld für seine ausgezeichnete Betreuung sowie sein großes Vertrauen. Herrn Professor Dr. Josef Bille danke ich für die Übernahme des Zweitgutachtens.

Herrn Professor Dr. Wolfgang Schlegel möchte ich für die Möglichkeit der Durchführung meiner Arbeit in seiner hervoragend ausgestatteten Abteilung danken. Ebenso gilt mein Dank allen Mitarbeitern für die angenehme Atmosphäre innerhalb der Abteilung und die Hilfsbereitschaft bei der Beantwortung all meiner Fragen.

Besonderen Dank schulde ich PD. Dr. Uwe Oelfke für die enge Zusammenarbeit und seine ständige Bereitschaft, mich durch allerlei Gespräche, trotz unterschiedlicher Dialekte, meinem Ziel näher zu bringen.

Bedanken möchte ich mich auch noch bei meinen vielen Zimmerkollegen der letzten Jahre. An erster Stelle sei hier Herrn Dr. Burkhard Groh gedankt. Durch seine dauerhafte positive und offene direkte Art, meine Fragen zu beantworten, bin ich um so manche Erfahrung reicher. Frau Luciana Pavel sowie den Herren Klaus Borkenstein, Christian Thieke und Christian Scholz sei an dieser Stelle für Ihre Geduld und Hilfsbereitschaft gedankt. Dr. Mike Partridge danke ich für sein sorgfältiges Korrekturlesen der englischen Sprache.

I would like to thank Dr. Mikael Karlsson und Lennart Olofsson for supplying me with the electron pencil beam kernels.

Der Firma MRC, insbesondere Dr. Mark-Aleksi Keller-Reichenbecher und Herrn Micha Weber, möchte ich für die gute Zusammenarbeit bei allen softwaretechnischen Problemen danken.

Ich bedanke mich beim Deutschen Akademischen Austauschdienst für die Finanzierung meines Forschungsaufenthaltes am Massachusetts General Hospital in Boston, Massachusetts. Dank auch an Dr. Wayne Newhauser für die zeitweise Unterbringung und sonstige manigfaltige Hilfe während meines Aufenthalts am MGH.

Zum Schluss möchte ich meinen Eltern danken, die mich in allen Phasen dieser Arbeit begleitet und alles getan haben, um mich dabei zu unterstüzen.